LATVIAN JOURNAL of PHYSICS and TECHNICAL SCIENCES

ISSN 0868 - 8257

3

(Vol. 56)

2019

SATURS

CONTENTS

СОДЕРЖАНИЕ

LATVIAN JOURNAL of PHYSICS and TECHNICAL SCIENCES

LATVIJAS FIZIKAS un TEHNISKO ZINĀTŅU ŽURNĀLS

ЛАТВИЙСКИЙ ФИЗИКО-ТЕХНИЧЕСКИЙ ЖУРНАЛ

Published six times a year since February 1964
Iznāk sešas reizes gadā kopš 1964. gada februāra
Выходит шесть раз в год с февраля 1964 года

3 (Vol. 56) • 2019

RĪGA

INDEKSĒTS (PUBLICĒTS) | INDEXED (PUBLISHED) IN

www.scopus.com
www.sciendo.com
EBSCO (Academic Search Complete, www.epnet.com), INSPEC (www.iee.org.com).
VINITI (www.viniti.ru), Begell House Inc/ (EDC, www.edata-center.com).

Izdevēji: Fizikālās enerģētikas institūts, LU Cietvielu fizikas institūts
Reģistrācijas apliecība Nr. 000700221
Redakcija: Krīvu iela 11, Rīga, LV-1006
Tel. 67551732
e-pasts: ezerniec@edi.lv
Interneta adrese: www.fei-web.lv

sciendo

LATVIAN JOURNAL OF PHYSICS
AND TECHNICAL SCIENCES
2019, N 3

DOI: 10.2478/lpts-2019-0015

PHYSICAL AND TECHNICAL ENERGY PROBLEMS

DESIGN OF A THREE-PHASE BIDIRECTIONAL PWM RECTIFIER WITH SIMPLE CONTROL ALGORITHM

K. Frisfelds, O. Krievs
Institute of Industrial Electronics and Electrical Engineering,
Riga Technical University,
12/1 Azenes Str., Riga, LV-1048, LATVIA
e-mail: Kaspars.Frisfelds@inbox.lv

The paper covers the main aspects of designing a low voltage three-phase PWM rectifier for bidirectional AC/DC power flow with unity power factor. A model in Matlab/Simulink environment has been built for a 10kW active rectifier with an LCL filter connected to grid side of the rectifier. The primary goal of the model is to achieve low grid current harmonic content for frequency ranges described in worldwide applicable standards and above. LCL filter parameter design procedure is described in the paper and implemented in the rectifier model to achieve a better power quality with limitations in passive element size. A simple ‘’p-q” theory-based voltage oriented control algorithm is used in the model and described in the present paper. Model performance is characterised by dynamic response, stability and grid parameters during simulation. The simulation results demonstrate that the modelled rectifier system is stable and the grid current harmonic content is low both in the low- and high-frequency ranges.

Keywords: *bi-directional AC/DC rectifier, LCL filter*

1. INTRODUCTION

Bidirectional AC/DC power flow converter or three-phase pulse-width-modulation (PWM) rectifier is a rapidly developing research field since different applications of various kinds of DC micro-grids evolve considerably. Interfacing DC systems to AC distribution grids by means of uncontrolled rectifiers often creates unacceptable voltage and current distortion in the AC grid. Moreover, many DC micro-grid systems incorporate DC power sources (e.g., renewables, regenerative braking of electrical machines), which in some cases require passing electrical energy back to the AC grid [1]–[3].

The goal of the paper is to design a three-phase bidirectional rectifier model with input current in the limits of regulated standards, such as IEEE 519-1992. A

third-order low-pass LCL filter will be designed as the current ripple attenuation is very effective for limited inductor sizes with the capacitor impedance inversely proportional to the frequency of the grid current. LCL filter will be designed to attenuate low and high (around switching frequency) order harmonics [4], [5]. Rectifier control will be implemented with synchronously rotating *dq* frame to control load current d and q axis components and active/reactive power separately and maintain a constant DC link voltage during dynamic load changes. Matlab/Simulink environment will be used to design the rectifier and simulate the behaviour during different operation modes. The model is built such that afterword an experimental setup using dSpace platform is possible.

2. SIMULATION STUDY

The designed rectifier model is shown in Fig. 1. Apart from the main full-bridge circuit, this topology also includes a 3-phase grid network with accordant grid impedance parameters L_{source}, LCL parameters L_{filter}, L, C_f, R_d and DC link capacitor C_{dc}. Load is changed with DC side resistance $R_{dc1,}$ external DC source is used to test the model in inverter mode.

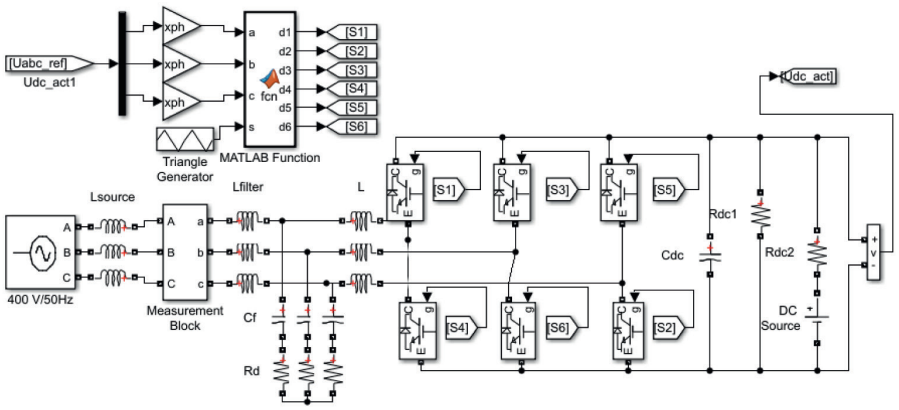

Fig. 1. Basic structure of designed PWM rectifier.

Inductors connected between the input of the rectifier and line bring the current source character of the input circuit and provide boost feature of the rectifier. The line current i_L is controlled by the voltage drop across the inductance L interconnecting line and rectifier voltage sources. By controlling the phase angle and amplitude of rectifier voltage, phase and amplitude of line current are indirectly controlled [3].

With a larger DC side capacitor, smaller LCL filter inductance and smaller voltage loop proportional gain k_{vp}, the rectifier will be more stable. A larger capacitance will lead to a slower dynamic response of the converter, so a tradeoff between system stability and other performances must be made [6].

LCL filter configuration produces better attenuation of switching harmonics than L and LC filters [4]. With an LCL filter, it is possible to use relatively low switching frequency for a given harmonic attenuation. The gained attenuation of LCL filter is 60dB/decade in excess of the resonance frequency according to [7].

The resonant frequency of the LCL filter is given by:

$$f_0 = \frac{1}{2\pi}\sqrt{\frac{\left(L_{filter} + L\right)}{L_{filter} \cdot L \cdot C_f}}. \quad (1)$$

LCL filter may cause both dynamic and steady state input current distortion due to resonance [7]. If a third-order LCL filter is proper designed – resonant frequency is far away from both fundamental AC frequency and switching frequency, it is possible to eliminate the line current ripple and the switching noise at low switching frequencies with smaller inductor than with L or LC filters. Generally, all LCL filter design approaches, which are introduced in papers [8], [9], [4] are similar. The mentioned papers show great results in simulation and experimental tests.

The procedure for choosing the LCL filter parameters uses the power rating of the converter, the line frequency, and the switching frequency as input. Filter must be properly damped. LCL filter capacitor value is limited by a decrease in the power factor at rated power (less than 5 %). The total value of LCL filter inductance is limited to 0.1 pu [8].

After calculation described in [8], LCL filter parameters are shown in Table 1. The LCL filter is connected to a grid of inductance according to a 75 MVA three-phase transformer. Capacitor on the DC side of the converter is chosen to ensure that DC voltage fluctuations do not exceed 1 %.

Table 1

LCL Filter Parameters for the Designed Model

Source inductance, L_{source}, mH	0.135
Grid side inductance, L_{filter}, mH	1
Converter side inductance, L, mH	1
Filter capacitor, C_f, μF	2.2
Damping resistor, Rd, Ω	15.55
DC capacitor capacitance, Cdc, μF	6500
Switching frequency, fs, Hz	15000
Sampling frequency, fsampling, Hz	30000
Rectifier nominal power, Pn, W	10000
Grid voltage, Vl, V	400

Resonant frequency is kept in the range between ten times the line frequency and one half of the switching frequency to avoid resonance problems in lower and upper parts of harmonic spectrum. The network frequency f_n is 50Hz, switching frequency f_{sw} is 15 kHz. The resonant frequency f_0 of 4603 Hz satisfies this requirement.

The Matlab/Simulink model control (Fig. 3) uses a closed loop current control in a rotating reference frame – voltage oriented control (VOC) topology described in [3]. Current feedback is managed from the rectifier side. As a model in *abc*-frame cannot realise a zero steady state error for PI controller with time variant variables, three-phase stationary frame is transformed into the synchronously rotating *dq* frame [6].

Coordinate transformation of current and voltage to rotating *dq*-coordinates (Park transformation) is done by a Simulink block that transforms a three-phase signal to rotating *dq*-coordinates with the grid angular frequency *w*, and *d* axis aligned with grid voltage vector (Fig. 2). The variables in *dq*-coordinates are DC quantities and PI controller can provide zero steady state error control.

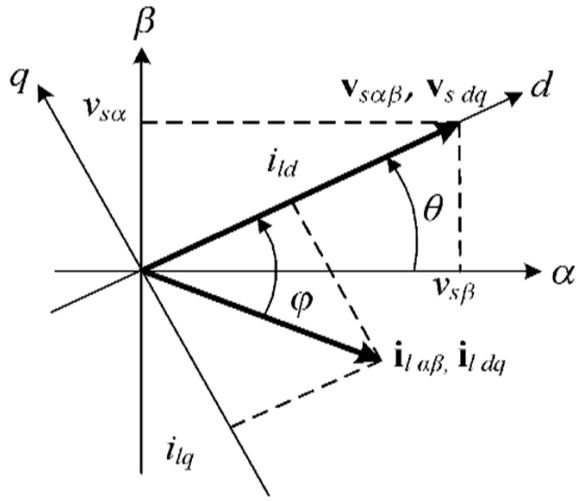

Fig. 2. Load current and grid voltage phasors in Clark's and Park's reference frames.

The PWM rectifier model in *dq*-frame can be obtained as follows, according to [3], [6]:

$$V_{Ld} = L\frac{di_{Ld}}{dt} - w \cdot L \cdot i_{Lq} + e_d \tag{2}$$

$$V_{Lq} = L\frac{dil_{Lq}}{dt} + w \cdot L \cdot i_{Ld} + e_q \tag{3}$$

$$C\frac{dV_{dc}}{dt} = \left(i_{Ld} \cdot S_d + i_{Lq} \cdot S_q\right) - i_{DC}\,, \tag{4}$$

where e_d, e_q, i_{Ld} and i_{Lq} are grid voltage and current, V_{Ld}, V_{Lq} are voltages at the rectifier terminals in *dq*-frame. $V_{Ld}=S_d \cdot V_{dc}$, $V_{Lq}=S_q \cdot V_{dc,}$ S_d and S_q are components of the switching function and i_{DC} is the DC link current [6].

Rectifier control consists of double-loop control (Fig. 3). The outer loop is DC voltage loop and the inner are current loops. Task of current loops is to perform regulation of converter's currents along *d* and *q* axis to control active and reactive power independently as i_{Lq} determines the reactive power, i_{Ld} determines the active power flow [10]. Task of the voltage loop is to keep the DC link voltage constant and at a value to keep the diodes of the converter blocked and maintain the controller stability – 700V. The voltage control loop controls the active energy flow and compensates the active losses of the converter.

For the DC voltage loop, the command DC voltage V_{DC_ref} is compared with the measurement of actual DC voltage V_{DC_act}, the error is delivered to PI controller UDC_PI, which stabilises DC voltage and generates an output signal or command active current i_d^*, therefore regulating the active power of the converter. Reactive current command i_q^* is set to 0 in order to achieve a unity power factor. Command currents can be expressed as follows:

$$\begin{cases} i_d^* = k_{vp}\left(V_{DC\_ref} - V_{DC\_act}\right) + k_{vi}\int \left(V_{DC\_ref} - V_{DC\_act}\right)dt \\ i_q^* = 0, \end{cases} \tag{5}$$

where k_{vp}, k_{vi} represent proportional and integral factors of voltage loop.

Command active and reactive currents are compared with their measured values from Clark transformation block I_d and I_q and errors are delivered to the respective PI controller. To generate V_d^* and V_q^* references, output of the PI controller is compared with the actual values of measured V_d, V_q voltages and the voltage drop on filter, source and converter side inductances in order to decouple d and q axis. A first-order low-pass filter set to passband edge frequency 628 rad/s eliminates high frequency noise from V_d^* and V_q^*, expressed as follows [3],[6]:

$$\begin{cases} V_d^* = V_d + w \cdot L \cdot i_q - k_{ip}(i_d^* - i_d) - k_{ii}\int (i_d^* - i_d)dt \\ V_q^* = V_q - w \cdot L \cdot i_d - k_{ip}\left(i_q^* - i_q\right) - k_{ii}\int \left(i_q^* - i_q\right)dt \end{cases} \tag{6}$$

where k_{ip}, k_{ii} represent proportional and integral factors of current loop.

Commands V_d^* and V_q^* are transformed to *abc*-frame to generate switching signals of IGBTs locked to the grid voltage vector by phase angle of line voltage determined by PLL block in Simulink. Control signals of upper and lower power switch in the same bridge arm are turned on complementarily to avoid short circuit on the DC side [3],[6],[11].

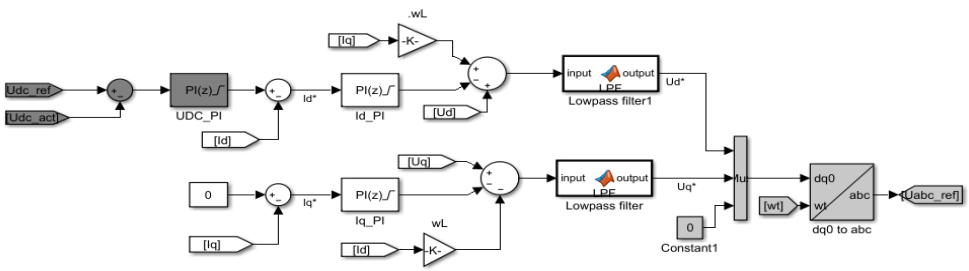

Fig. 3. Control system in Simulink environment.

3. RESULTS

In order to validate the selected control approach and developed topology, a simulation in MATLAB/Simulink environment is carried out with parameters shown in Table 1. Simulation for rectifier input current distortion is carried out with the power consumption in rectifier and inverter mode set to 10kVA. Grid (at point of common coupling) and converter (between LCL filter and rectifier) current waveforms in rectifier mode are illustrated in Fig. 4.

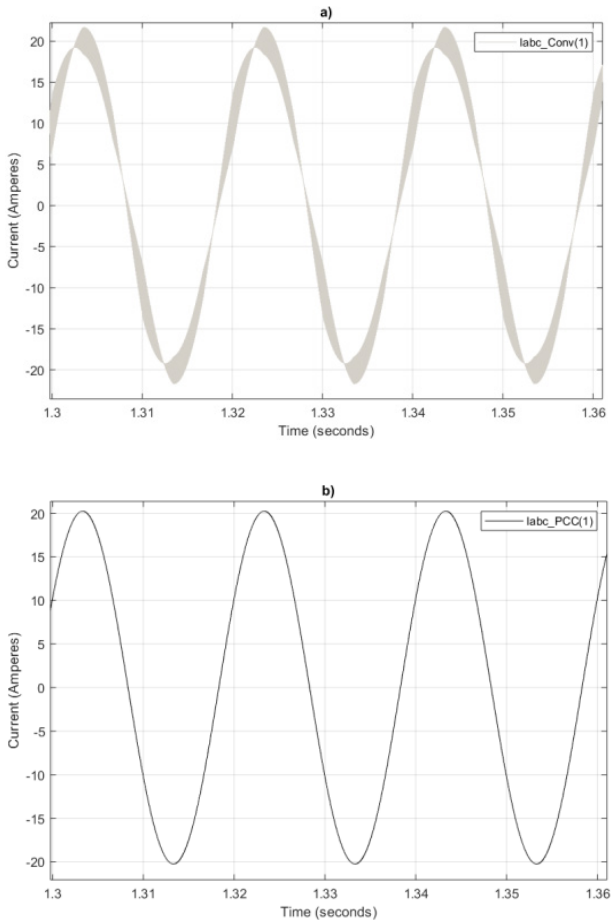

Fig. 4. Converter – a, Grid – b, current waveforms for phase A with load set to 10kVA, during rectifier mode.

The current is purely sinusoidal and in phase with the grid voltage as can be seen in Fig. 5 during rectifier mode and in phase but negative during inverter mode.

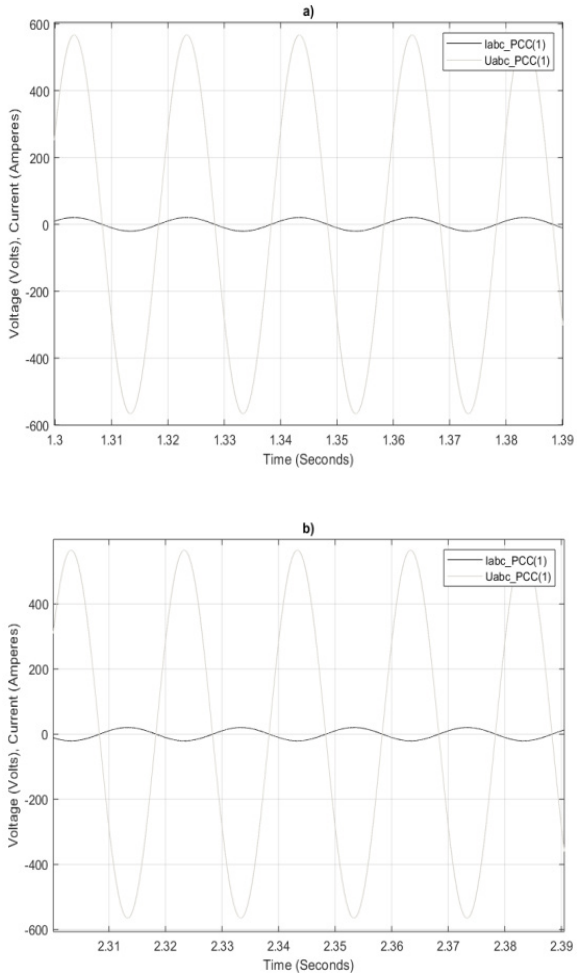

Fig. 5. Grid current and voltage waveforms for phase A with load set to 10kVA during a – rectifier mode, b – inverter mode.

Grid and converter current harmonic spectrum with the dominating harmonic orders is illustrated in Table 2. The THD of the grid current in rectifier mode with nominal load is 0.37 % and 0.34 % in inverter mode, and complies with IEEE-519 (THD<5 %). As can be seen from Fig. 4 and Table 2, the LCL filter is effective in attenuating harmonics around switching frequency *h*=296, 298.

Table 2

Grid and Converter Current Harmonic Spectrum

	THD, %	h=5	h=7	h=296	h=298
I_{grid} rectifier mode	0.37	0.01	0.01	0.02	0.37
$I_{converter}$ rectifier mode	12.43	0.07	0.04	2.38	12.18
I_{grid} inverter mode	0.34	0.01	0.01	0.02	0.34
$I_{converter}$ inverter mode	11.48	0.07	0.03	2.19	11.25

To ensure the dynamic response of PWM rectifiers, load is changed during simulation and rectifier is set to work as an inverter since an external voltage is connected to the DC side.

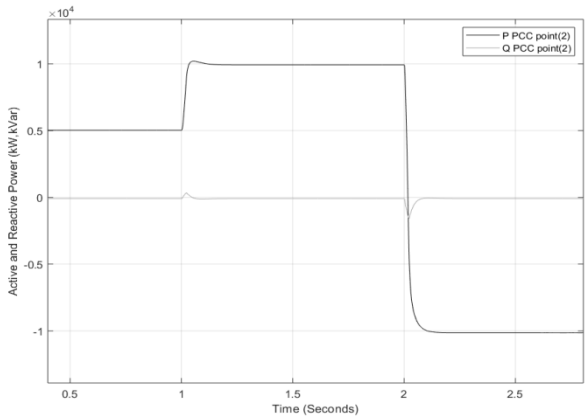

Fig. 6. Active and reactive power consumption at point of common coupling.

As can be seen from Fig. 6, the converter is able to compensate reactive power in rectifier and inverter modes. After an external voltage source is connected, the converter operates as inverter and power is delivered to grid, hence, the negative value of active power after 2 seconds.

Control of the converter effectively regulates the DC link voltage and stabilizes it after load changes as can be seen in Fig. 7.

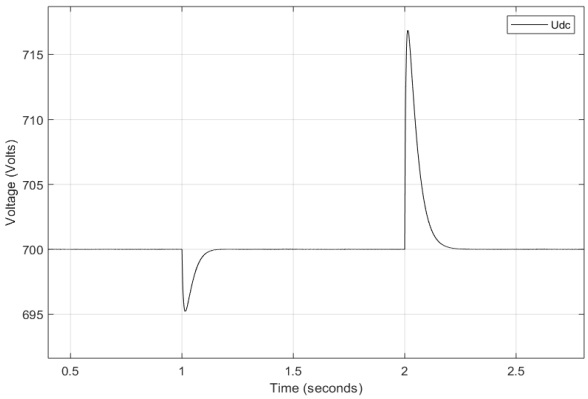

Fig. 7. DC link voltage during load change.

4. CONCLUSIONS

Model of a bidirectional PWM rectifier has been implemented in Matlab/ Simulink environment in order to validate the power circuit design considerations as well as the proposed simple control method. The PWM rectifier can operate as a rectifier or inverter with grid current distortion lower than the applicable standards (THD=0.4 % in rectifier mode and THD=0.3 % in inverter mode). The designed LCL filter effectively attenuates high switching frequency harmonics. The control method

is capable of compensating reactive power and maintaining the DC link voltage even during rapid load variations. Since the simulation results confirm effectiveness of the proposed control method, the algorithm in Matlab/Simulink environment will further be used for experimental validation with a dSpace real time interface control platform and a 10kVA laboratory prototype of a PWM rectifier.

ACKNOWLEDGEMENTS

This research is funded by the Ministry of Economics of the Republic of Latvia, project RTUAER, project No. VPP-EM-AER-2018/3-0004.

REFERENCES

1. Suhara, E. M., & Nandakumar, M. (2015). Voltage oriented control of three phase PWM rectifier with Bus Clamped Space Vector PWM. *2015 International Conference on Power, Instrumentation, Control and Computing (PICC)*, 1–5. DOI: 10.1109/PICC.2015.7455788
2. Wu, X., Panda, S. K., & Xu, J. (2007). Analysis and experimental validation of the output voltage and input current performances in three phase PWM boost rectifiers under unbalanced and distorted supply voltage conditions. *2007 IEEE International Conference on Control Applications*. 605–610. DOI: 10.1109/CCA.2007.4389298
3. Kazmierkowski, M. P., Krishnan, R., & Blaabjerg, F. (2002). *Control in Power Electronics. Selected Problems.* USA: Elsevier Science.
4. Nuilers, S., & Neammanee, B. (2010). Control performance of active damp LCL filter of three phase PWM boost rectifier. *ECTI-CON2010: The 2010 ECTI International Conference on Electrical Engineering/Electronics, Computer, Telecommunications and Information Technology*, 259–263.
5. Malinowski, M., & Bernet, S. (2008). A simple voltage sensorless active damping scheme for three-phase PWM converters with an LCL filter. *IEEE Transactions on Industrial Electronics*, *55*(4), 1876–1880. DOI: 10.1109/TIE.2008.91706
6. He, S., Xiong, J., & Dai, D. (2018). Modeling and stability analysis of three-phase PWM rectifier. *2018 IEEE International Power Electronics and Application Conference and Exposition (PEAC)*, 1–5. DOI: 10.1109/PEAC.2018.8590508
7. Ahmed, K. H., Finney, S. J., & Williams, B.W. (2007). Passive filter design for three-phase inverter interfacing in distributed generation. *Journal of Electrical Power Quality and Utilisation*, 13(2), 1–9. DOI: 10.1109/CPE.2007.4296511
8. Liserre, M., Blaabjerg, F., & Hansen, S. (2005). Design and control of an LCL-filter-based three-phase active rectifier. *IEEE Transactions on Industry Applications*, *41*(5), 1281–1291. DOI: 10.1109/TIA.2005.853373
9. Kantar, E., Usluer, S.N., & Hava, A.M. (2013). Control strategies for grid connected PWM-VSI systems. *2013 8th International Conference on Electrical and Electronics Engineering (ELECO)*, 220–224. DOI: 10.1109/ELECO.2013.6713835
10. Akagi, H., Watanabe, E.H., & Aredes, M. (2007). *Instantaneous Power Theory and Applications to Power Conditioning*. New Jersey, USA: John Wiley & Sons.
11. Wei, G., Hongchao, J., & Xingwu, Y. (2014). A three-phase PWM rectifier with reactive power compensation function. *2014 IEEE PES Asia-Pacific Power and Energy Engineering Conference (APPEEC)*, 1–4. DOI: 10.1109/APPEEC.2014.7066073

TRĪSFĀZU AKTĪVĀ TAISNGRIEŽA AR VIENKĀRŠOTU VADĪBAS ALGORITMU IZPĒTE UN IZSTRĀDE

K.Frišfelds, O.Krievs

K o p s a v i l k u m s

Raksts veltīts trīsfāzu aktīvā IPM taisngrieža izstrādei, kas spētu nodrošināt divvirzienu elektroenerģijas plūsmu ar pilnībā aktīvu ieejas jaudas koeficientu. Rakstā piedāvāta vienkāršota aktīvā IPM taisngrieža sprieguma vadības metode un izstrādāts tā datormodelis Matlab/Simulink vidē. Iegūtie modelēšanas rezultāti apliecina, ka piedāvātā vadības metode nodrošina stabilu taisngrieža darbību pat pie dinamiskām slodzes pārmaiņām un efektīvu darbu gan taisngrieža, gan invertora režīmos. Taisngrieža ieejas strāvas harmonisko kropļojumu koeficients (THD) pie pārveidotāja nominālās slodzes ir 0.4 % taisngrieža režīmā un 0.3 % invertora režīmā, kas atbilst IEEE-519 standarta prasībām. Ar piedāvāto vadības algoritmu turklāt iespējama maiņsprieguma puses aktīvās un reaktīvās jaudas regulēšana. Ieejā pieslēgtais LCL filtrs efektīvi vājina ieejas strāvas augstākās harmoniskās komponentes IPM komutācijas frekvences apgabalā. Turpmākais darbs paredz Matlab/Simulink vidē izstrādātā vadības algoritmu pielietošanu 10kVA aktīvā taisngrieža eksperimentālā prototipa vadībai, izmantojot dSpace reālā laika vadības platformu.

08.04.2019.

sciendo

LATVIAN JOURNAL OF PHYSICS
AND TECHNICAL SCIENCES
2019, N 3

DOI: 10.2478/lpts-2019-0016

MAGNETOSTRICTIVE VIBRATION MODEL FOR EVALUATION OF MECHANICAL INTEGRITY OF POWER TRANSFORMER MAGNETIC CORE

J. Marks, S.Vitolina, J. Dirba
Riga Technical University,
12/1 Azenes Str., Riga, LV-1048, LATVIA
e-mail: janis.marks@edu.rtu.lv

Magnetostriction process creates vibrations within magnetic core of a power transformer. This effect can cause delamination of magnetic core layers and increase the vibration amplitudes on the surface of transformer tank. In this paper, a magnetostrictive vibration model is proposed for improved evaluation of the mechanical integrity of magnetic core and the finding of possible mechanical defects. This model is based on the simulation of magnetostrictive vibrations by replacing the magnetic core with mass and spring system, and application of a dynamic genetic algorithm in order to find the necessary system configuration. A case study is provided structurally modelling magnetic core in *Matlab* and *Matlab Simulink* with the analysis of simulated vibrations that indicate a possible mechanical defect.

Keywords*: magnetostriction, numerical simulation, transformer cores.*

1. INTRODUCTION

There are numerous different defects that can originate within power transformers during their operation period. These defects can be categorized in the following types:

- Electrical defects – e.g., internal short-circuits between individual winding turns, localized partial discharges;
- Thermal defects – e.g., transformer winding solid insulation degradation, hot spots in transformer windings;
- Mechanical defects – e.g., loosening and displacement of windings, delamination of magnetic core layers.

This paper focuses on mechanical defects within the magnetic core of a power transformer.

There are multiple diagnostic approaches that are designed to detect mechanical

defects. Vibroacoustic method uses information from the vibrations registered on the surface of transformer tank. This method is mainly used to diagnose mechanical defects in transformer windings since it determines the existence of a mechanical defect, if vibration amplitude values for a set position are elevated. However, by measuring individual harmonic amplitudes of registered vibrations, this method can diagnose the possibility of a mechanical defect within magnetic core, if the certain harmonic amplitudes are elevated as well, although this approach cannot detect the position and intensity of a mechanical defect [1]. Another power transformer diagnostics method is a sweep frequency response analysis (SFRA). This approach can detect changes within the windings and magnetic core of a power transformer by observing the change for multiple given frequency domains of transformer response [2]. However, by applying this approach, it is not possible to detect the position of mechanical defect beyond a single phase of the transformer as well as the severity of it. Furthermore, this method requires a baseline data information in order to operate.

The aim of this paper is to develop an approach to better evaluate the mechanical integrity of magnetic core of power transformers and to determine whether a possible mechanical defect exists by proposing a magnetostrictive vibration model.

2. MAGNETOSTRICTION EFFECT

In general, the geometrical changes in length caused by magnetostriction occur if the material is composed of microscopic domains that each have their individual magnetic poles. This is true for ferromagnetic materials. If no external magnetic field is applied, the polar direction of these domains is redistributed randomly throughout the given material. However, if an external magnetic field is applied to the given material, the domains begin to alter their magnetic polarity. The result of this reaction is that the domains that originally were aligned with the external field have increased in size and the remaining domains have diminished in size. Figure 1 illustrates the effect of this process. The magnitude of this process is dependent of the strength of the externally applied magnetic field but has a diminishing effect. [3]. The physical effect of the magnetostriction process is the source of vibration generation. This is due to the fact that microscopic domains are not perfect spheres.

Magnetostriction effect is the cause of mechanical movement within the magnetic core of the power transformer and it occurs because this component is made of ferromagnetic material and during the operation of transformer there is a constantly changing magnetic field propagating throughout the magnetic core. This process causes the magnetic core to change its dimensions and emit vibrations [4], [5]. The nature of this movement is periodic and proportional to the primary voltage frequency since the generated magnetic field has also periodically changing values and is induced by the primary voltage [6]. Therefore, magnetic core exhibits vibrations, which are then transmitted through other mechanical elements of the power transformer until they reach the surface of the tank. This is a complicated process because the vibration distribution path has multiple components.

The change in length for the direction aligned with the magnetic field is different from the same effect in perpendicular direction [8], [9]. This is due to the shape of magnetic

domains of material and the lamination of magnetic core [10]. The correlation between applied magnetic field strength and the caused deformation is dependent on the material used since the magnetic domains can have different molecular structure and, therefore, geometrical shapes [11], [12].

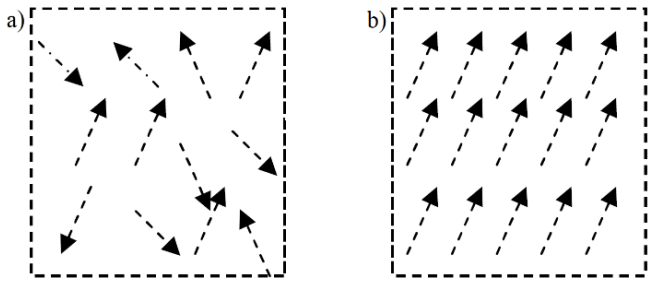

Fig. 1. Magnetic domain alignment (a) with no external magnetic field, (b) with external magnetic field [7].

The negative consequences of magnetostriction effect are emitted noise, which can exceed given limits and delamination of the magnetic core layers over a long period of time of continuous operation [7], [13], [14]. Created vibrations from the magnetic core may overlap the vibrations caused by the windings due to electrodynamic forces and, therefore, make it difficult to detect mechanical defects within it.

2. THE PROPOSED MAGNETOSTRICTIVE VIBRATION MODEL

To detect a mechanical defect and to improve evaluation of vibration measurement data, the authors have developed a power transformer mechanical vibration generation model caused by magnetostriction effect in magnetic core. The flowchart of the proposed model is displayed in Fig. 2 and this vibration simulation approach is interlinked with the previous research for winding mechanical defect detection [15].

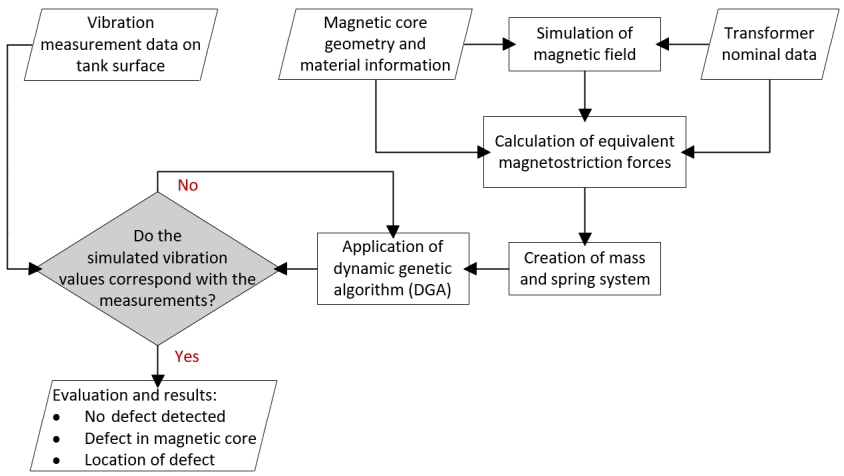

Fig. 2. Evaluation of mechanical integrity of magnetic core by magnetostrictive vibration model.

The proposed model is based on the replacement of magnetic core with mass and spring system that is moved by equivalent forces of magnetostriction effect. Furthermore, the model applies a dynamic genetic algorithm (DGA) in order to find the correct spring stiffness coefficients to create a configuration of coefficients for the mass and spring system that is capable of producing vibrations corresponding to the measurements of vibration total value on tank surface. The equivalent forces required to move this system are calculated by using the magnetostriction deformations and the Young's modulus of the magnetic core material.

Figure 3 illustrates how the magnetic core is replaced with a system of mass elements connected internally with springs. The alignments of springs are constructed in order to have each individual mass element connected with 6 springs, 2 springs for each dimension axis. This is required since all mass elements need to be capable of movements in any direction. This is achieved by combining the movements in each dimension axis as part of superposition.

It should be noted that all existing springs are not visible in Fig. 3. The hidden springs connect mass elements of magnetic core outer boundaries to other elements of the transformer structure. These structural fragments are assumed to be stationary and do not create vibrations of their own. Furthermore, the mass elements displayed in gray tone are defined as stationary as well since these regions of magnetic core have better fastenings and, therefore, do not exhibit vibrations caused by magnetostriction with equal intensity. Corresponding positions of vibration sensors providing vibration total value measurement data on tank surface are displayed in dashed pattern. Furthermore, this replacement approach is applicable to any form of magnetic core as well as to power transformers with different rated power.

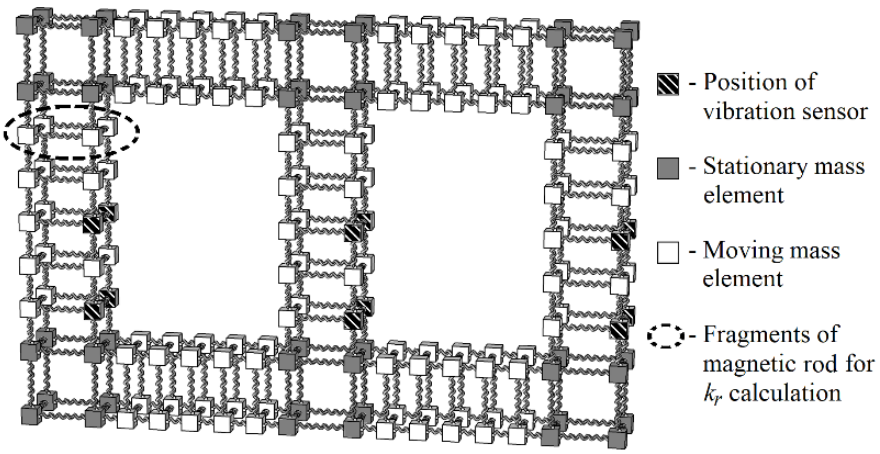

Fig. 3. Magnetic core representation as mass and spring system.

When magnetostriction effect exerts a force upon a given mass element, the surrounding springs create a force in the opposite direction. However, the new equilibrium point in space for this mass element has changed, thus, movement occurs as a result to this change. Therefore, by applying a periodic force on the mass element, vibrations are generated. Figure 4 illustrates the movement of a single mass element in vertical axis and the resulting forces acting upon it as a result.

For this mass and spring system to operate, it is necessary to generate forces caused by a magnetostriction effect. A simple movement of mass element due to magnetostriction does not suffice since this process does not have a single vectoral direction. This is because the change in mass element length due to magnetostriction in a single axis will not move the centre of mass but expand or contract the element itself. However, the sides of the mass element will change their position. Therefore, deformations caused by magnetostriction cannot be expressed as forces that produce a movement of the whole mass element.

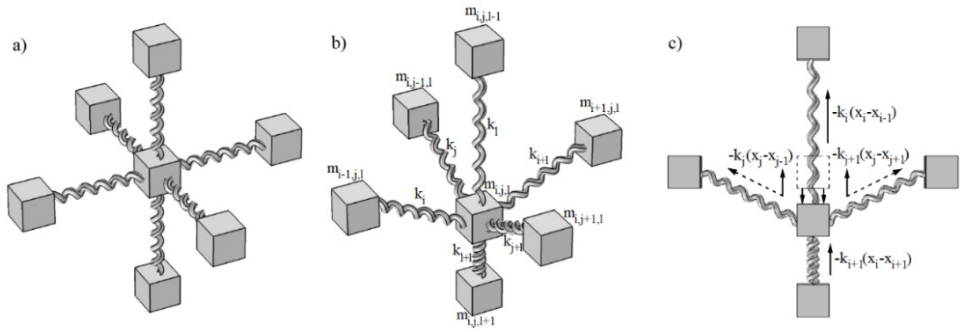

Fig. 4. (a) Mass element connection with neighbouring elements, (b) spring deformation due to element movement and (c) the acting elastic forces upon the displaced mass element.

For this reason, it is proposed to use Young's modulus of the magnetic core material in order to acquire forces that produce equivalent overall mass element movement as a magnetostriction effect.

Equation (1) describes the calculation of Young's modulus

$$E = \frac{F \cdot l_0}{S \cdot \Delta l}, \tag{1}$$

where F applied force, N;
l_0 initial length of the material, m;
S surface area, where the force is applied, m^2;
Δl deformation length of the material, m.

The change in length Δl of magnetic core due to magnetostriction can be expressed as a function based on the magnetic induction value of the externally applied magnetic field [16]. This function is usually represented as a magnetostriction graph that illustrates the correlation between magnetic induction values and caused change in length for electrical steel both in direction aligned to the magnetic induction vector and perpendicular to it [17]. However, due to the nature of these graphs being symmetric, the correlation between magnetic induction and deformation can be approximated and expressed as functions, displayed in equations (2) and (3)

$$\Delta l_d = \frac{346.23 \cdot B^6 - 1410.6 \cdot B^4 - 420.71 \cdot B^2 - 79.301}{10^9} \quad (2)$$

$$\Delta l_p = \frac{-86.659 \cdot B^6 + 84.198 \cdot B^4 - 2027.6 \cdot B^2 - 105.9}{10^9}, \quad (3)$$

where Δl_d material length change in parallel direction, m;
Δl_p material length change in perpendicular direction, m;
B magnetic induction, T.

Thus, the change in magnetic core dimensions is based on the magnetic induction value and direction at any part of the entire geometry of the magnetic core. This process creates difficulties to model the entire magnetic core as a single solid material since the values and direction of magnetic induction are different in any part of the magnetic core geometry and are changing throughout time. Therefore, it is possible to calculate the applied force to a mass element since all other variables of equation (1) can be acquired. This is possible because the initial dimensions of the mass element are defined. Therefore, both surface area S and initial length l_0 are known. The deformation values Δl_d and Δl_p can be calculated by using magnetostriction functions described in equations (2) and (3), and the values of Young's modulus for electrical steel are known and displayed in Table 1.

Table 1

Young's Modulus Absolute and Relative Values of Electrical Steel [18], [19]

Direction	*E* value, Pa	Relative *E* value to steel, %
Parallel to magnetic field	$157 \cdot 10^9$	78.5
Perpendicular to magnetic field	$104 \cdot 10^9$	52
Perpendicular to lamination	$176 \cdot 10^9$	88

Therefore, it is possible to calculate the equivalent forces to a magnetostriction effect in both parallel and perpendicular directions to all axial components of a magnetic induction vectoral value by using equation (1) and expressing the force value *F* from it. Together there are three force values for one magnetic induction axial component since the effect of magnetostriction exists in all three axial directions. Therefore, it is necessary to add all force values in a single direction from all three magnetic induction axial components to obtain the values of $F_{xl}(t)$, $F_{yl}(t)$ and $F_{zl}(t)$ required in equations (4), (5) and (6) that describe the movement of each mass element in three dimensions by applying Newton's second law of motion and the effect of stiffness coefficients of systems springs

$$m_i \cdot \frac{d^2 x_i}{dt^2} - k_{xi} \cdot \left(x_{i-1} - \frac{x_i}{2}\right) - k_{xi+1} \cdot \left(x_{i+1} - \frac{x_i}{2}\right) - k_{yj} \cdot \left(x_{j-1} - x_j\right)$$
$$-k_{yi+1} \cdot \left(x_{j+1} - x_j\right) - k_{zl} \cdot (x_{l-1} - x_l) - k_{zl+1} \cdot (x_{l+1} - x_l) = F_{xi}(t) \quad (4)$$

$$m_j \cdot \frac{d^2 y_j}{dt^2} - k_{yj} \cdot \left(y_{j-1} - \frac{y_j}{2}\right) - k_{yi+1} \cdot \left(y_{j+1} - \frac{y_j}{2}\right) - k_{xi} \cdot (y_{i-1} - y_i)$$
$$-k_{xi+1} \cdot (y_{i+1} - y_i) - k_{zl} \cdot (y_{l-1} - y_l) - k_{zl+1} \cdot (y_{l+1} - y_l) = F_{yj}(t) \quad (5)$$

$$m_l \cdot \frac{d^2 x_l}{dt^2} - k_{zl} \cdot \left(x_{l-1} - \frac{x_l}{2}\right) - k_{zl+1} \cdot \left(x_{l+1} - \frac{x_l}{2}\right) - k_{yj} \cdot \left(x_{j-1} - x_j\right)$$
$$-k_{yi+1} \cdot \left(x_{j+1} - x_j\right) - k_{xi} \cdot (x_{i-1} - x_i) - k_{xi+1} \cdot (x_{i+1} - x_i) = F_{xi}(t) \text{ , } (6)$$

where m_i; m_j; m_l mass of the corresponding element, kg;

$k_i \ldots k_{l+1}$ stiffness coefficient of springs in corresponding position;

$x_{i-1} \ldots x_{l+1}$; $y_{i-1} \ldots y_{l+1}$; $z_{i-1} \ldots z_{l+1}$ position of the centre of mass element in corresponding position and direction, m;

$F_{xi}(t)$; $F_{yj}(t)$; $F_{zl}(t)$ applied force to the mass element in corresponding direction, m.

By applying equations (4), (5) and (6) to the mass and spring system, it is possible to calculate the position, speed and acceleration of each mass element. However, the model needs to find mass element movements that generate vibrations equal to those measured on the tank surface of the transformer. Therefore, the stiffness coefficients of the springs must be adjusted. The possible number of combinations of stiffness coefficients for the springs is too large to compute all the possibilities since only applying integer values between 10^4 and 10^7 with a system of 84 springs has in total approximately 9.194^{587} individual combinations. Therefore, it is impossible to use a brute force approach and, thus, dynamic genetic algorithm (DGA) is applied.

The DGA creates a randomized combination of spring stiffness coefficients and calculates the generated vibration values. This process simulates a single individual of a population of possibilities. For DGA to be able to find an acceptable result, multiple individuals must be simulated. They create a population for a single generation of configuration evolution. After all individuals are simulated and their vibration results calculated, the individuals are sorted based on their vibration results corresponding to the required values. This difference between calculated and measured vibration values is the fitness function of the DGA. Then, a random number of individuals are deleted and reproduced by the surviving ones. However, the new individuals have randomized changes to their structure – mutations. Both the deletion and reproduction processes are partly randomized. However, there is a gradient approach used as based in the previous research [15]. The better the fitness function of an individual compared to the corresponding population, the smaller

the change of this individual to be deleted and larger the change of reproduction form of this individual. Therefore, this process improves the fitness function of each generation of population and simulates evolution.

Over multiple generations, the fitness function becomes acceptable and the calculated vibration values correspond to the measured values. Therefore, the internal stiffness coefficient structure is obtained for the mass and spring system to generate the required vibration values. This process is performed to vibration values for both sides of each magnetic core rod or yoke. Afterwards, the stiffness coefficients of the generated system's internal structure are compared to search for differences, and ratio coefficient k_r is calculated as $k_r = k_{rmax}/k_{rmin}$, i.e., a result from dividing the largest value stiffness coefficient k_{rmax} by the smallest value stiffness coefficient k_{rmin} of a given fragment of magnetic core. Each fragment consists of 4 mass elements forming a square grid with the length of it aligned with measured vibration direction. Figure 3 displays these fragments as horizontal layers of mass elements in the structure of each rod.

The value of k_r shows if the stiffness coefficients of springs aligned with the vibration direction and positioned next to each other differ. High value of k_r shows evidence of a possible mechanical fault within this fragment of magnetic core since the mechanical integrity of this component is lowered and it exhibits loose structural components. However, k_r value close or equal to 1 signifies that corresponding stiffness coefficients represent a homogenous structure with no relatively loose elements, thus, there is no evidence of a mechanical defect.

3. CASE STUDY

A power transformer is used as a case study in order to confirm that the proposed magnetostrictive vibration model is operating as intended. Figure 5 displays the measured vibration visualization to the corresponding positions on the tank surface of the selected transformer in no-load operation. Lower part of phase A at high voltage side indicates elevated vibration displacement amplitudes that are marked in a darker tone. Furthermore, there are areas on the magnetic core, with no tone coding added where vibration measurements were not taken.

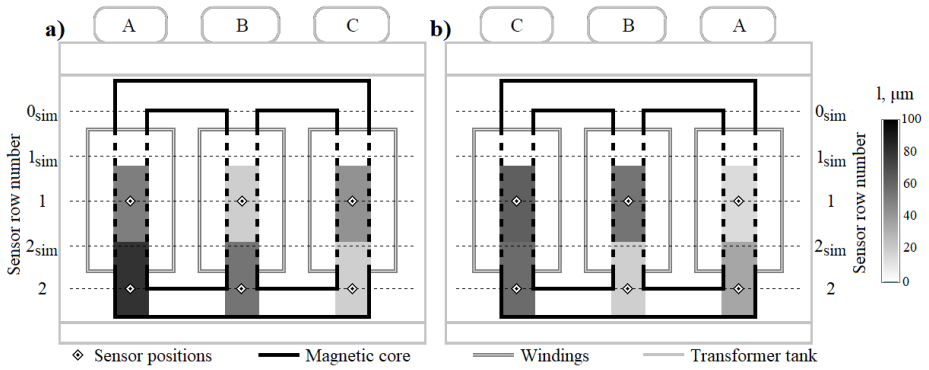

Fig. 5. Measured vibration visualization to their corresponding positions for (a) high voltage side and (b) low voltage side.

For this case study, *Matlab* and *Matlab Simulink* software is used to create the proposed magnetostrictive vibration model. Each of the magnetic core rods is replaced with a mass and spring system consisting of 20 individual mass elements internally connected with 84 springs. The visualization of this approach is displayed in Fig. 3. Equations (4), (5), and (6) are created as signal feedback loops. Each of the 20 mass elements have a feedback loop for the calculation of position and movement in a single direction. Therefore, 3 equation replacements with this approach simulate mass element movement within three-dimensional space. Figure 6 displays a single feedback loop. The initial input parameters are as follows:

- the equivalent magnetostrictive forces, *F(x)t1* block;
- mass of the element, *m1* block;
- spring stiffness coefficients surrounding the element, all blocks starting with the letter "*k*".

It should be noted that all feedback loops simulating magnetostrictive vibrations are connected since the position of neighbouring mass elements impact the movement of the original mass element.

In this case study, DGA generated an evolution that consisted of a population of 500 individuals over 80 generations for each of the magnetic core rods. The generated result has good conformity with the vibration values measured on the surface of the transformer tank since the calculated RMS error total value is 2.04 % across all simulated vibration positions in all magnetic core rods. Figure 7 illustrates the graphical interpretation of this comparison, where dashed lines indicate vibration measurement results and continuous lines – simulated vibration results.

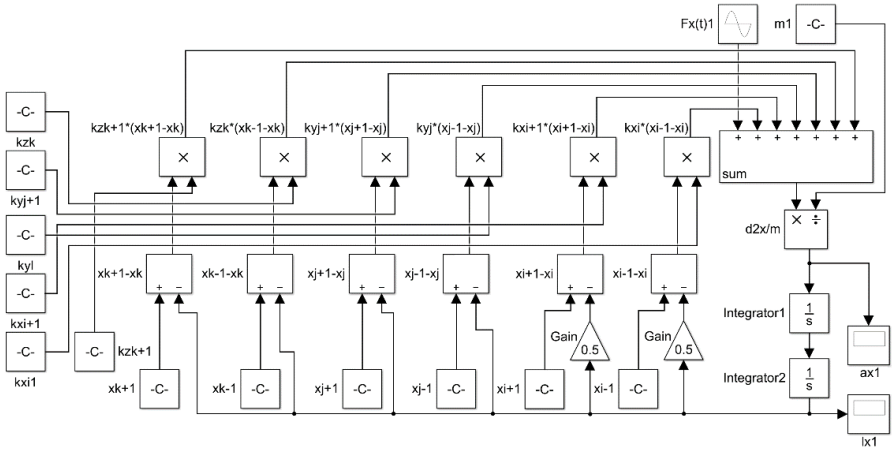

Fig. 6. Mass element movement calculation block for a single dimension, *Matlab Simulink*.

It should be noted that the original vibration measurements are limited to the magnetic core rod middle and lower regions. However, the proposed model created and extrapolated results for the unknown positions as well. These vibration displacement amplitude values at the top of the magnetic core rod have the corresponding nature to the values at lower structure sectors since they are within the range of the same magnitude of amplitudes.

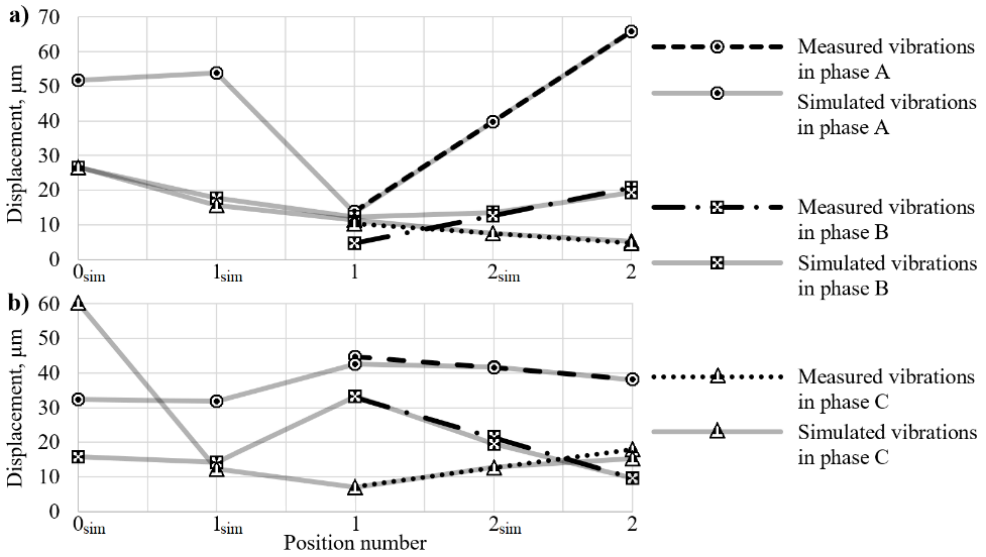

Fig. 7. Simulated and measured vibration values for (a) high voltage side and (b) low voltage side.

Afterwards, the values of ratio coefficient k_r are calculated as described in Section 3. Table 2 shows the acquired results throughout all magnetic core rods at every measured sensor row corresponding to sensor row number 1 and 2, as well as interpolated results between the sensor rows marked as 2_{sim} and extrapolated results located at the top regions of rods named 0_{sim} and 1_{sim}.

Table 2

Calculated Resulting Values of k_r

Row no.	Values of k_r		
	Phase A	Phase B	Phase C
$_{0si}$m	1	4	5
1_{sim}	102	2	1
1	4	1	3
2_{sim}	3	2	2
2	27	12	1

The values of k_r for phase C exhibit typical structural behaviour consistently diminishing towards upper fragments of rod. However, increased values of k_r can be observed both at upper and lower regions of the rod of phase A, as well as at the lower region of phase B. That indicates decreased mechanical integrity in this area of magnetic core since the vibration simulation results show that there are fragments within these rods that have loose structural components.

4. CONCLUSIONS

The proposed magnetostrictive vibration model investigates replacing the magnetic core of a power transformer with a mass and spring system and applying a dynamic genetic algorithm in order to create a black box of numerous spring stiffness coefficients to simulate vibrations corresponding to the vibration measurements made on a tank surface.

The obtained stiffness coefficients of the mass and spring system are used to evaluate if there is a defect within the magnetic core.

The power transformer for the case study was selected since there were mechanical defects found during the diagnostics process. Implementation of the proposed model indicated that there was evidence of mechanical defects within magnetic core rods of phases A and B, thus confirming that the proposed magnetostrictive vibration model was operating as intended.

ACKNOWLEDGMENTS

The paper has been developed within the framework of doctoral studies grant of Riga Technical University (34-11200-DOK.EI/18).

REFERENCES

1. Borucki S., Fracz P., Boczar T., & Zmarzly D. (2012). Diagnostics of Power Transformers Cores Using a Modified Vibroacoustic Method. In: *2012 IEEE International Symposium on Electrical Insulation*, Jun. 2012, San Juan, USA, DOI: 10.1109/ELINSL.2012.6251453.
2. Aravinda G.A.T.N., Bandara k., Jayantha G.A., Kumara J.R.S.S., & Fernando M.A.R.M. (2017). Application of SFRA Techniques to Discriminate Short Circuit Faults of Transformer Winding. In: *2017 IEEE International Conference on Industrial and Information Systems (ICIIS)*, Feb. 2017, Peradeniya, Sri Lanka, DOI: 10.1109/ICIINFS.2017.8300409.
3. Yuan C., Gao X., Li J., Mu X., & Bao X. (2015). Magnetic Domain Motion and Magnetostriction in the Fe–Ga Sheets. *IEEE Transactions on Magnetics*, 51(11), DOI: 10.1109/TMAG.2015.2442294.
4. Zhang P., Li L., Cheng Z., Tian C., & Han Y. (2019). Study on Vibration of Iron Core of Transformer and Reactor Based on Maxwell Stress and Anisotropic Magnetostriction. *IEEE Transactions on Magnetics,* 55(2), DOI: 10.1109/TMAG.2018.2875017.
5. ZhangY., Wang J., Sun X., Bai B., & Xie D. (2014). Measurement and Modeling of Anisotropic Magnetostriction Characteristic of Grain-Oriented Silicon Steel Sheet under DC Bias. *IEEE Transactions on Magnetics*, 50(2), DOI: 10.1109/TMAG.2013.2281599.
6. Hilgert T., Vandevelde L., & Melkebeek M. (2008). Comparison of Magnetostriction Models for Use in Calculations of Vibrations in Magnetic Cores. *IEEE Transactions on Magnetics*, 44(6), DOI: 10.1109/TMAG.2007.916395.
7. Yusuf A., Amoo, A., Aliyu, U., Mustafa, M.W., & Zin, A.A.M. (2012). Magnetostriction Assessment of Power Transformer (A Case Study of 30/40MVA, 132/33 kV Transformer at Bauchi Substation). In: *2012 IEEE International Power Engineering and Optimization Conference Melaka, Malaysia*. Jun. 2012, Melaka, Malaysia, DOI: 10.1109/PEOCO.2012.6230845.

8. Ghalamestani, S.G., Vandevelde, L., & Melkebeek, J.A.A. (2016). Magnetic Forces and Magnetostriction in Rotating Electrical Machines. In: *2016 XXII International Conference on Electrical Machines (ICEM)*, Sept. 2016, Lausanne, Switzerland, DOI: 10.1109/ICELMACH.2016.7732840.
9. Somkun, S., Moses, A.J., & Anderson, P.I. (2012). Measurement and Modeling of 2-D Magnetostriction of Nonoriented Electrical Steel. *IEEE Transactions on Magnetics*. 48(2), 711–714, DOI: 10.1109/TMAG.2011.2173302.
10. Dirba, J., & Ketners, K. (2009). *Electrical Machines*. Riga: RTU Press. (in Latvian).
11. Bormio-Nunes, C., Serra, J. P., Barbosa, F. S., Dias, M. B. S. Turtelli, R. S., Atif, M., & Größinger, R. (2016). Magnetostriction of Fe-Cr and Fe-Cr-B alloys. *IEEE Transactions on Magnetics,* 52(5), DOI: 10.1109/TMAG.2015.2512271.
12. Wun-Fogle, M., Restorff, J.B., Cuseo, J.M., Garshelis, I.J., & Bitar, S. (2009). Magnetostriction and Magnetization of Common High Strength Steels. *IEEE Transactions on Magnetics,* 45(10), 4112–4115, DOI: 10.1109/TMAG.2009.2021531.
13. Gao, Y., Nagata, M., Muramatsu, K., Fujiwara, K., Ishihara, Y., & Fukuchi, S. (2011). Noise Reduction of a Three-Phase Reactor by Optimization of Gaps between Cores Considering Electromagnetism and Magnetostriction. *IEEE Transactions on Magnetics*, 47(10), 2772–2775, DOI: 10.1109/TMAG.2011.2154378.
14. Chang, Y., Hsu, C., Chu, H., & Tseng, C. (2011). Magnetomechanical Vibrations of Three-Phase Three-Leg Transformer with Different Amorphous-Cored Structures. *IEEE Transactions on Magnetics*, 47(10), 2780–2783, DOI: 10.1109/TMAG.2011.2154378.
15. Marks, J., & Vitolina, S. (2018). Dynamic Genetic Algorithm in Model for Vibrations of Power Transformer Windings. In: *2018 International Conference and Exposition on Electrical and Power Engineering (EPE),* Oct. 2018, Iasi, Romania, DOI: 10.1109/ICEPE.2018.8559932.
16. Jang, P., & Choi, G. (2012). Acoustic Noise Characteristics and Magnetostriction of Fe-Si Powder Cores. *IEEE Transactions on Magnetics*, 48(4), 1549–1552, DOI: 10.1109/TMAG.2011.2173563.
17. Zhang, Y., Wang, Y., Zhang, D., Ren, Z., & Xie, D. (2016). Research on Magnetostriction Property of Silicon Steel Sheets. *International Journal of Energy and Power Engineering*, 5(1), 65–74, DOI: 10.11648/j.ijepe.s.2016050101.20.
18. Giet, M., Kasper, K., Doncker, R.W., & Hameyer, K. (2012). Material parameters for the structural dynamic simulation of electrical machines. In: *2012 XXth International Conference on Electrical Machines*, Sept. 2012, Marseille, France, DOI: 10.1109/ICElMach.2012.6350314.
19. Beckley, P. (2002). *Electrical Steels for Rotating Machines*. London: The Institution of Engineering and Technology.

MAGNETOSTRIKTĪVU VIBRĀCIJU MODELIS SPĒKA TRANSFORMATORU MAGNĒTVADA MEHĀNISKĀS IZTURĪBAS NOVĒRTĒŠANAI

J. Mārks, S.Vītoliņa, J. Dirba

K o p s a v i l k u m s

Izpētīta magnetostrikcijas efekta ietekme uz lieljaudas transformatoru magnētvadu, radot tā presējuma atslābšanu ekspluatācijas laikā. Lai uzlabotu magnētvada mehāniskās izturības novērtēšanu un vibrāciju mērījumu rezultātu uz transformatora tvertnes virsmas interpretāciju, ir piedāvāts magnetostrikcijas radīto vibrāciju ģenerēšanas modelis. Modelis paredz magnētvadu aizstāt ar masu un atsperu sistēmu, kurā iekšējo masu elementu kustību ģenerē magnetostrikcijas efektam ekvivalenti spēki, kā arī ir pielietots dinamisks ģenētiskais algoritms, lai atrastu pareizu modelētās masu un atsperu sistēmas konfigurāciju. Gadījuma izpētes iegūtie rezultāti rada aizdomas par iespējamu mehānisku defektu esamību modelētā transformatora magnētvadā.

12.04.2019.

sciendo

LATVIAN JOURNAL OF PHYSICS
AND TECHNICAL SCIENCES
2019, N 3

DOI: 10.2478/lpts-2019-0017

UTILISATION OF THE SAFETY INDEX (ELMERI INDEX) AS THE OSH INDICATOR AT COAL MINES

Marat L. Rudakov*, Elena B. Gridina, Vyacheslav S. Ershov
Department of Industrial Safety
Saint-Petersburg Mining University
199106, 2 21st Line, St. Petersburg, RUSSIA
*e-mail: Rudakov_ML@pers.spmi.ru

The article describes the main performances of the global coal industry, as well as key occupational safety and health indicators (OSH indicators) of the coal mining industry of the Russian Federation. The main goal of the article is to present the results of research of potential utilisation of the Elmeri observation method in order to evaluate safety levels at underground coal mines. The investigation performed taking into consideration two root causes of the occupational traumatism (methane and/or dust explosions, as well as rock falls) has demonstrated good correlation between the calculated values of the safety index and results of the risk assessments at the same underground coal mine under consideration. In addition, the article includes a brief discussion of advantages and restrictions in respect of utilisation of the safety index as the OSH monitoring tool at coal mines.

Keywords: *coal production, dangers, methane explosions, observation, occupational fatalities, rock fall, safety indicator*

1. INTRODUCTION

In 2017, coal consumption increased by 25 million tonnes of oil equivalent (mtoe) or by 1 % – it was the first growth since 2013 in accordance with the BP Statistical Review of World Energy [1]. World coal production has grown by 105 mtoe or by 3.2 % – it has been the fastest rate of growth since 2011. Production has grown by 56 mtoe in China and by 23 mtoe in the US. In 2016–2017, approximately 90 % of the global coal production was ensured by 7 leading coal-mining countries (China, the USA, Australia, India, Indonesia, the Russian Federation, and South Africa). Occupational safety and health issues in the coal industry still demand for attention and action because high rates of occupational accidents and diseases still remain the major source of concern. They influence productivity and competitiveness, as well as social protection systems.

As far as Russia is concerned, improvements in the sphere of the OSH have led to a decrease in fatal injuries in the coal mining industry. In accordance with the report of the Federal Environmental, Industrial and Nuclear Supervision Service of Russia, there is a clear tendency towards a decrease in the total number of the major industrial accidents and occupational fatalities in the coal mining industry (Fig. 1).

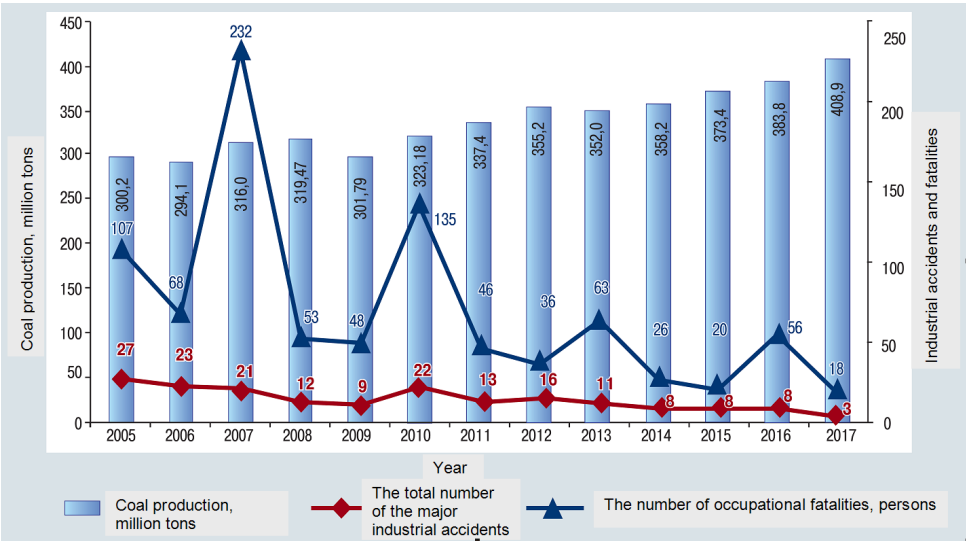

Fig. 1. Dynamics of coal production, the number of the major industrial accidents and occupational fatalities in the coal mining industry of Russia.

Source: Federal Environmental, Industrial and Nuclear Supervision Service of Russia http://en.gosnadzor.ru/

In 2017, the quantity of fatal accidents decreased by 67.8 % as compared with 2016; total quantity of accidents decreased from 304 accidents in 2016 to 118 accidents in 2017. In 2017, the value of the specific indicator of fatal traumatism, which is calculated as the quantity of workers with fatal injuries per million tons of the coal extracted during a year, decreased from 0.14 to 0.04 person/million tons as compared with 2016.

Despite the fact that there were no major industrial accidents, which were caused by the methane/air explosions at the underground coal mines in Russia in 2017 (Fig. 2), these explosions could result in the extremely high observed level of individual risks at certain enterprises. For example, the level of the employees' death risk increased up to $9.1 \cdot 10^{-3}$ at Ulyanovskaya Coal Mine in 2007; up to $2.8 \cdot 10^{-3}$ at Severnaya Coal Mine in 2016, and up to $1.7 \cdot 10^{-3}$ at Raspadskaya Coal Mine in 2010 [2].

The necessity of implementation of measures in the sphere of occupational safety of workers of coal mines requires taking into consideration all key factors, which influence the safety (for example, such injury risk factors as gas and/or dust explosions; sudden outbursts of rock, gas and/or dust; rock bumps; inbursts of water to the underground mining workings; spontaneous endogenous fires; rock falls). At present, estimates of the injury risks of workers at coal mines are made with the help of various methods and systems, which make it possible to estimate the risk both due

to influence of certain dangerous factors [2]–[3] and the risk due to joint influence of these factors [4]–[8].

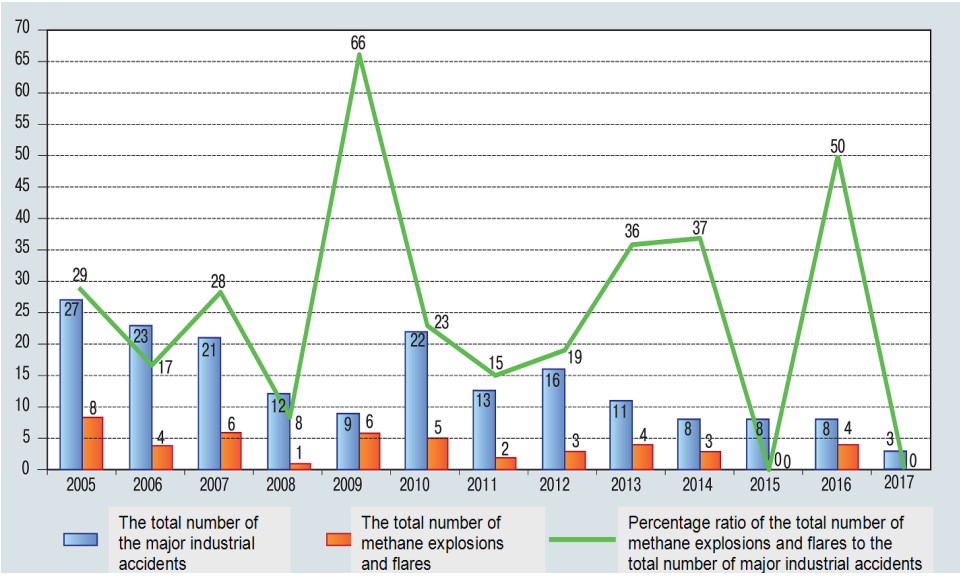

Fig. 2. Dynamics of the total number of the major industrial accidents and methane explosions/flares at the underground coal mines in Russia.

Source: Federal Environmental, Industrial and Nuclear Supervision Service of Russia http://en.gosnadzor.ru/

2. METHODOLOGY

The idea of the method for estimation of the safety level, which was developed by the governmental supervisory institutions of Finland along with the number of leading construction corporations, is as follows. In accordance with the results of observations over the factors of the production environment grouped according to certain characteristics, results are entered to the relevant questionnaire based on the principle "correct" or "not correct" ("+" or "–", "complies with" or "does not comply with"). State of the object of observation (of a certain factor of the production environment) is considered "good", and "+" sign is entered to the relevant information field, if this object complies with the minimum level of the safety requirements. If the state of the object does not comply with the requirements of the labour protection, then "–" sign is entered. If there are no possibilities to estimate this factor or if it cannot be revealed with the help of the method of observation (for example, the level of the air dustiness), then "is absent" or "0" signs are entered to the relevant information field of the observation card.

The level of safety at the object of observation (at the work place, within a structural division, or within the entire organisation) is estimated with the help of the so-called safety index (SI; other names and close names: Elmeri index, safety

coefficient, “TR-barometer”, “WS-barometer”), which is expressed as percentage and which makes it possible to make generalised estimations in respect of the degree of compliance of the observation object with the labour protection requirements.

$$SI = \frac{No.\ of\ correct items}{No.of\ correct items + No.of\ not correct items} \cdot 100\% . \quad (1)$$

Therefore, in the case of application of this method in the construction industry, it is envisaged to perform observations over 6 groups of factors at each work place within the construction site: production process; framing scaffold, overpass ramp, trestle stand, and portable ladders; safety of labour in the course of work with machines and facilities; individual fall arrest facilities; electric networks and illumination facilities; cleanness and order at the work place.

As it follows from formula (1), the safety index is the percentage ratio, value of which can change from 0 % (complete incompliance with the safety requirements) up to 100 % (complete compliance with the safety requirements). For example, the result at the level of 60 % shows that 60 points of 100 estimated points comply with the labour protection requirements.

At present, the method, which is based on calculation of the numerical safety index (Elmeri index), is considered the simplest indirect method of the quantitative assessment of risks, which is successfully applied to various branches of industry [9]–[13]. Article [14] describes the method of estimation of production risks on the basis of ranking safety requirements. In addition, this article includes a formula for calculation of the safety index in respect of the coal mines of the Kuznetsk Basin. The basis of this method is as follows: it is necessary to determine interrelation between the assembly of the safety requirements, which are complied with, and all existing requirements – governmental normative requirements (which are denoted with the help of letter “N”); objectively important requirements (letter “I”); recommendatory requirements (letter “R”).

In order to calculate safety index SI on the basis of the main injury risk factors of the coal mines in operation, we have used the methodological recommendations [8], which present the list of all main hazards that are grouped in 6 clusters on the basis of analysis of the statistical data in respect of the accident rate and traumatism within the coal industry of Russia: hazard due to gas and/or dust explosions; hazard due to sudden outbursts of coal, gas and/or dust; hazard due to rock bumps; hazard due to inbursts of water to the underground mining workings; hazard due to endogenous fires; hazard due to rock falls; hazard due to influence of the “subjective” factor (human factor).

3. RESULTS

Calculation of the safety index SI has been made on the basis of the data in respect of operation of the productive coal mine within the territory of the Russian Federation. In accordance with the results of analysis of reasons of the industrial

traumatism, it was established that injuries/traumas of workers were caused, for the most part, by methane or dust explosions, as well as by rock falls. Therefore, the safety index was calculated in the following manner. At the first stage of this calculation, it was necessary to reveal the observed factors, which influenced the hazard of the gas and/or dust explosion (Table 1).

Table 1

Example of Insertion of Relevant Signs to the Table of those Factors, which Have Influence upon the Hazard of the Gas and/or Dust Explosion

Factor under observation	Correct	Not correct
Were explosions (flares) of the gaseous methane registered?		+
Were explosions (flares) of the gaseous methane and the coal dust registered?	+	
Forecasts in respect of the methane bleeding is performed automatically	+	
Registration of forecasts in respect of the methane bleeding is performed manually	+	
Availability of other explosive gases (H_2S, NH_3, H_2, higher hydrocarbons)	+	
Is coal dust in the mine explosive?		+
Recording of gas contaminations of the mine openings during the last year		+
Availability of air within the mine		+
Aerological protection within the framework of the multifunctional safety system	+	
Aerogas control (hereinafter referred to as the AGC) within the general mine openings	+	
AGC within the main fan installation and the mine-gas-drainage plant	+	
AGC within the developing section	+	
AGC within the extraction district/working area		+
Availability of the complex degassing system	+	
Availability of the dust-explosion protection system within the general mine openings	+	
Availability of the dust-explosion protection system within the developing section	+	
Availability of the dust-explosion protection system within the extraction district/working area		+
Availability of the dedusting installation (according to the irrigation technique) within the loading point	+	
Availability of the dedusting installation (according to the irrigation technique) in the course of shaft excavation	+	
Availability of the dedusting installation (according to the irrigation technique) within the mine face	+	
Total: 22 factors that influence the hazard of methane and/or dust explosion	16	6

The safety index in respect of this hazard is equal to:

$$SI = \frac{16}{16+6} \cdot 100\% = 73\%$$

At the second stage of this calculation, it was necessary to reveal the observed factors influencing the hazard of the rock falls (Table 2). Availability of the factors, which have positive influence upon the safety level, was fixed with the help of "+" ("Correct") sign, while availability of the factors posing negative influence upon the safety level was fixed with the help of "–" ("Not correct") sign.

Table 2

Example of Insertion of Relevant Signs to the Table of those Factors, which Have Influence upon the Hazard of the Rock Falls

Factor under observation	Correct	Not correct
Rock falls during three previous years		+
There are no coal seams with the unstable roof within this mine, no work operations are performed within the zones of the high rock pressure (hereinafter referred to as the HRP), as well as within the zones of influence of the geological boundary faults		+
The coal seams with the unstable immediate roof are developed within the mine, certain work operations are performed within the HRP zones		+
Essential part of work operations is performed within the HRP zones, as well as within the zones of influence of the geological boundary faults		+
The coal seams with the unstable immediate roof are developed within the mine, work operations are performed within the HRP zones and zones of influence of the geological boundary faults, thick coal seams are developed, there is the danger of the coal sloughing		+
Periodical instrumental/visual examination of the roof state	+	
Automated monitoring of the rock mass state within the framework of the multifunctional safety system	+	
Total: 7 factors that influence the hazard of the rock falls	2	5

The safety index in respect of this hazard is equal to:

$$SI = \frac{2}{2+5} \cdot 100\% = 28\%$$

It is obvious that the main efforts in the labour safety sphere at this mine must be connected with protection against the hazards of the rock falls. Total safety index in respect of these two hazards is equal to:

$$SI_{\Sigma} = \frac{16+2}{(16+6)+(2+5)} \cdot 100\% = 62\%$$

Therefore, it is possible to state that the degree of safety at this mine is not at the satisfactory level, and it is necessary to take urgent measures with the aim of industrial traumatism prevention.

4. DISCUSSION

With the aim of verification of the obtained results, we have made estimates of risks of the accident $\boldsymbol{R}$ at the mine under investigation with the help of the method, which is described in [8] in respect of the hazard of the gas and/or dust explosion, as well as the hazard of the rock falls. The results obtained were compared with the results of estimates of the risk $\boldsymbol{R_{SI}}$ in respect of the same hazards, provided that this risk was determined with the help of the safety index:

$$R_{SI} = 1 - \frac{SI}{100\%} = \frac{No.\ of\ not\ correct\ items}{No.of\ correct\ items + No.of\ not\ correct\ items} \qquad (2)$$

Figures 3 and 4 present comparative results of the estimates of the accident risks, which were obtained in accordance with the method [8] – $\boldsymbol{R}$, as well as the estimates, which were obtained with the help of the safety index $\boldsymbol{R_{SI}}$ in respect of the danger of the gas and/or dust explosion, as well as the hazard of the rock falls.

In accordance with the results of this comparison, it is possible to conclude that results of estimates of the risks obtained with the help of various methods are quite close to each other. In principle, this conclusion is consistent with the results that are presented in articles [9], [15], which have demonstrated an inverse dependence of the level of traumatism and disease incidence on the Elmeri index for the enterprise of various branches of industry.

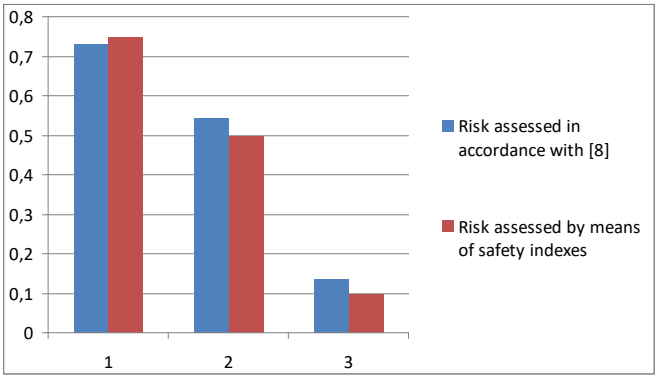

Fig. 3. The comparative graph of the risk estimates in respect of the hazard of the gas and/or dust explosion (both $\boldsymbol{R}$ and $\boldsymbol{R}_{SI}$ values were calculated at the same coal mines under investigation). X-axis: number of the coal mine investigated; Y-axis: risk estimates.

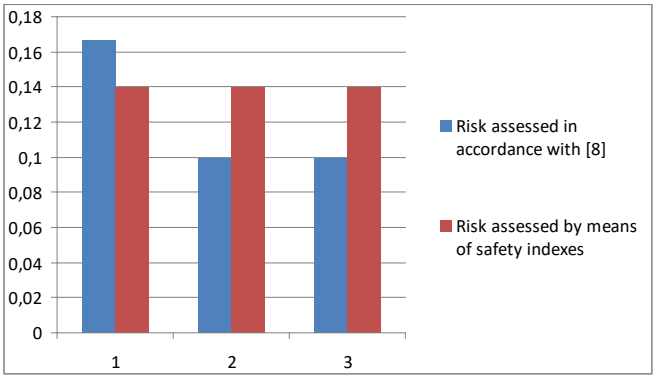

Fig. 4. The comparative graph of risk estimates in respect of the hazard of the rock falls (both $\boldsymbol{R}$ and $\boldsymbol{R}_{SI}$ were calculated at the same coal mines under investigation). X-axis: number of the coal mine investigated; Y-axis: risk estimates.

Therefore, the proposed method on the basis of the safety index makes it possible to estimate the total level of safety due to influence of certain hazards, as well as to substantiate implementation of the relevant events in the labour safety sphere in respect of the points, which are characterised as "bad" ones [16]. Therefore, in accordance with the results, which are presented in Table 1 and Table 2, it is possible to make a conclusion that the main efforts must be aimed at: recording of gas contaminations of the mine openings; dust-explosion protection within the extraction district and developing section; dedusting installation with the help of the irrigation technique within the mine face and in the course of shaft excavation; supervision over the roof state and state of the enclosing rocks within the mine openings; inspections and analysis of the information in respect of changes in the state of structure of the roof rocks; changes in the physical and mechanical properties of the roof rocks; characteristics of the rock-pressure manifestation. In addition, the above-proposed method makes it possible to perform estimates of the risks without more complicated methods of estimation, which are difficult for implementation at coal mines.

At the same time, simplicity of the proposed safety index method establishes certain restrictions in respect of application of this method by organisations of the coal industry:

1. As this method is based on observations, it does not make it possible to estimate a number of factors of the production environment, which have relevant influence upon the labour conditions of mineworkers (noise, physical overwork, dust concentration in the air of the work area etc.), and these factors require application of certain procedures of estimates, which are based on the instrumental measurements.
2. In the course of observations, it is assumed that all factors of hazards are equisignificant and they have no weighting coefficients. Therefore, it is not possible to estimate potential harm to the human health, which can be caused by the influence of these factors. However, the approach proposed in article [14], which envisages ranking factors by weights, in our opinion, can obstruct utilisation of the safety index in the working environment.
3. It is quite difficult to apply this method for the temporary work places, particularly in the cases of essential changes in the package of those factors, which influence relevant hazards.

5. CONCLUSIONS

Method of calculation of the safety index, which is based on observations, was applied from 2002 to 2005 both in the course of labour inspections and for the operating supervision over the state of safety at work places of enterprises of various types of economic activity. Additional advantage of this method is related to the possibility of its application in the working environment by the employees, who have no special qualification in the sphere of labour protection.

In accordance with the investigations performed, it is possible to state that this method, which is based on the calculation of "bad" and "good" points, can be used at coal mines in order to make: 1) estimates of the safety level of workers in respect of the safety index, and 2) express estimates of risks of the accidents. In the second case, risk must be calculated with the help of formula (2), which is derived from the formula for the sum of probabilities of opposite events.

It is worth underlining that this method does not make it possible to perform accurate estimations of the professional risks; however its simplicity enables us to recommend it for application in order to ensure quick estimates of the safety level at certain production departments of coal mines, for example, within the framework of supervision from the part of the trade union labour safety inspectors and other trade union activists, who are authorised to act in the occupational safety sphere.

REFERENCES

1. BP. (2018). *Statistical Review of World Energy*. Available at https://www.bp.com/en/global/corporate/energy-economics/statistical-review-of-world-energy.html

2. Smirnyakov, V.V., & F'en, N.M. (2018). Justification of a methodical approach of aerologic evaluation of methane hazard in development workings at mines of Vietanam. *Zapiski Gornogo instituta*, *230*, 197–203. doi: 10.25515/PMI.2018.2.197.
3. Korshunov, G.I., Rudakov, M.L., & Kabanov, E.I. (2018). Occupational safety and health in the sector of coal mining. *Journal of Environmental Management and Tourism*, *9*(1), 181–186.
4. Parchanski, J. (2016). Risk of injuries among coal mine workers and its hysteresis. *Journal of Mining Institute, 222*, 869–876. doi: 10.18454/PMI.2016.6.869.
5. Canbulat, I, Hoelle, J., & Emery, J. (2013). Risk management in open cut coal mines. *International Journal of Mining Science and Technology*, *23*, 369–374. doi: 10.1016/j.ijmst.2013.05.012.
6. Kirsch, P., Shi, M., & Sprott, D. (2014). Riskgate: industry sharing risk controls across Australian coal operations. *Australian Journal of Multi-Disciplinary Engineering*, *11*(1), 47–58. doi: 10.7158/14488388.2014.11464882
7. Kirsch, P., Harris, J., Sprott, D., & Cliff, D. (2014). Industry scale knowledge management – RISKGATE and Australian coal operations. *Canadian Institute of Mining Journal*, *5*(2), 79–86.
8. Order of the Federal Service for Environmental, Technological and Nuclear Supervision of June 5, 2017 No 192 "On approval of the Safety Guide" Guidelines for conducting hazard analysis and risk assessment of accidents in coal mines. Available at http://docs.cntd.ru/document/456073363
9. Laitinen, H., Vuorinen, M., Simola, A., & Yrjanheikki, E. (2013). Observation-based proactive OHS outcome indicators – Validity of the Elmeri+ method. *Safety Science*, *54*, 69–79. doi: 10.1016/j.ssci.2012.11.005.
10. Shah, N. (2015). Assessment of the workplace conditions and health and safety situation in chemical and textile industries of Pakistan. *Science Journal of Public Health*, *3*(6), 857–864. doi: 10.11648/j.sjph.20150306.20.
11. Jafari, A., Choobineh, A., Jahangiri, M., & Keshavarzi, S. (2017). An index developed for the assessment of occupational health and safety at workplace: A field study in a heavy automotive industry in the Northwest of Iran. *Health Sci. Surveillance Sys*., *5*(2), 86–93.
12. Pivnyak, G., Dychkovskyi, R., Bobyliov, O., Cabana, E.C., & Smoliński, A. (2018). Mathematical and geomechanical model in physical and chemical processes of underground coal gasification. *Solid State Phenomena*, *277*, 1–16.
13. Aleksandrov, V.M., Golozubenko, E.S., Ponomarev, S.A., & Saltykov, V.V. (2018). Detachment of alluvial paleofacial complexes in the upper Jurassic deposits of the South-West of the West Siberian oil and gas basin. *Periodico Tche Quimica, 15*(S1), 265–275.
14. Balovtsev, S.V., & Vorobyova, O.V. (2016). Management of production risks in coal mines based on ranking of safety requirements. *Mining Information and Analytical Bulletin*, *12,* 15–20.
15. Lozynskyi, V.G., Dychkovskyi, R.O., Falshtynskyi, V.S., Saik, P.B., & Malanchuk, Ye.Z. (2016). Experimental study of the influence of crossing the disjunctive geological fault on thermal regime of underground gasifier. *Naukovyi Visnyk Natsionalnoho Hirnychoho Universytetu*, *5*, 21–29.
16. Intima, D.P. (2017). Sampling plan for quality monitoring of suppliers of the sanitation sector. *Periodico Tche Quimica*, *14*(27), 39–43.

DROŠĪBAS INDEKSA (ELMERI INDEKSA) KĀ DARBA DROŠĪBAS UN VESELĪBAS RĀDĪTĀJA IZMANTOŠANA OGĻRAKTUVĒS

M. L. Rudakovs, E. B. Gridina, V. S. Eršovs

K o p s a v i l k u m s

Rakstā aprakstītas pasaules ogļrūpniecības galvenās darbības jomas, kā arī galvenie darba drošības un veselības rādītāji Krievijas Federācijas ogļrūpniecības nozarē. Raksta galvenais mērķis ir iepazīstināt ar Elmeri novērošanas metodes potenciālās izmantošanas izpētes rezultātiem, lai novērtētu drošības līmeni pazemes ogļraktuvēs. Pētījums, kas veikts, ņemot vērā divus darba traumatisma pamatcēloņus (metāna un/vai putekļu sprādzienus, kā arī akmeņu nogruvumu), ir pierādījis labu sakarību starp aprēķinātajām drošības indeksa vērtībām un riska novērtējuma rezultātiem apskatāmajās ogļraktuvēs. Rakstā arī ietverta īsa diskusija par priekšrocībām un ierobežojumiem attiecībā uz drošības indeksa izmantošanu kā darba drošības un veselības uzraudzības instrumentu ogļraktuvēs.

21.03.2019.

sciendo

LATVIAN JOURNAL OF PHYSICS
AND TECHNICAL SCIENCES
2019, N 3

DOI: 10.2478/lpts-2019-0018

IMPACT MODELLING OF EXPLOSION OF MIXTURE EXPLOSIVE CHARGES ON THE ENVIRONMENT

N. Remez[1], A. Dychko[1], Y. Besarabets[1], S. Kraychuk[2],
N. Ostapchuk[2], L. Yevtieieva[1]
[1] National Technical University of Ukraine
"Igor Sikorsky Kyiv Polytechnic Institute"
37 Peremohy Ave., Kyiv, 03056, UKRAINE
[2] Rivne State University of Humanities
12 Stepana Bandery Str., Rivne, 33000, UKRAINE

The present paper provides the modelling of the explosion of the charges of the traditional (trotyl) and new blended explosive substances: polymix GR1/8 (74 %) + KRUK2 (26 %), compolite GS6, polymix GR4-T10. As a result of the research, it has been established that when using TNT a specific impulse is formed, which is by 40 % more than an explosion of new mixed explosives, and the safe distance from the source of the explosion of such explosives is increased by 25 %–50 %. On the basis of the established dependences of excess pressure, the specific impulse on the type and mass of charge, as well as the distance from the epicenter of the explosion, an engineering method has been developed for calculating dangerous parameters of the explosion impact on the environment.

Keywords*: air shock wave, compolite explosives, destructive action, environment, explosion, modelling*

1. INTRODUCTION

Due to an increase in volumes of mining operations and coming of quarry fields to protected ecosystems, there is a question about their safety regarding intense dynamic loads during the explosion of explosives (EX). However, blasting operations are characterised by a small coefficient of explosive energy use, an increase in the requirements of technological and environmental safety, and the economic inactivity of the use of expensive industrial EX. Therefore, in recent years several tens of new non-TNT EX mixtures have been developed. At the same time, conclusions about their technological efficiency and environmental safety are based on visual observation of experimental and practical results of explosions.

Special attention should also be devoted to the territory where, in addition to environmental problems inherent in production processes, there are other types

of hazards, for example, related to the carrying out military operations (bombing, explosives of military stockpiles of ammunition, mines, the use of phosphate mines, the destruction of infrastructure of settlements, etc.). Therefore, scientists urgently raise the issue of the safety of natural-technogenic environment in the spread of airborne shock waves.

In this regard, the study of parameters of airborne shock waves (ASW) affecting the protected ecosystems in the explosions of new blended EX, and prediction of the degree of damage of technogenic systems and living organisms represent actual scientific and practical tasks.

2. LITERATURE REVIEW AND PROBLEM STATEMENT

As it is known, the main parameters of the airborne shock wave (ASW), which determine its destructive and demaging effect, are excess pressure ΔP, Pa; speed pressure ΔPs, Pa; specific pressure impulse I, Pa*s; time of shock wave action, τ_+, ms.

Excess pressure at the front of the shock wave is the main parameter that determines the destructive force of the shock wave. This is the difference between the maximum *P* and the atmospheric pressure P_0: $\Delta P = P - P_0$.

For the determination of excess pressure in engineering practice, various modifications of the empirical formula of M.A. Sadovsky [1], [2], used for charge of TNT, are widely implemented. For other explosives, the so-called energetic TNT-coefficient is used to determine the equivalence of the explosive. However, these formulas do not correspond to the theory of dimensions and similarity; therefore, their application can lead to unsatisfactory results.

The works of many scientists are devoted to the research into the definition and assessment of the impact of airborne shock waves. Most of the research focuses on the underground and terrestrial explosions and examines the damaging factors of a nuclear explosion. Methods for determining the individual parameters of the explosion and assessing their impressive impact on objects of the environment during the explosion are developed by Ya.M. Eisenberg, A.N. Birbaer, V.V. Boyko, O.O. Vovk, K.V. Yegupov, Yu.I. Kalyukh, M.A. Klyachko, S.V. Polyakov, Yu.I. Nemchinov, O.A. Savinov, A.E. Sargsyan, P.Z. Lugovoi, V.G. Kravets, V.S. Kukunaev, N.S. Remez, L.R. Stavnetsar, A.G. Tyapin, V.G. Bezdenkov, A.M. Trofimchuk, A.M. Uzdin, S.G. Shulman, N. Newmark, E. Rosenblueit and others.

The research of these scientists established such damaging for environment factors as funnel on the surface of the ground, the impact of the explosive shock wave, the seismic effect of the explosion on objects, the impact of the gas-dust cloud raised in the air during the explosion, thermal radiation, and the damaging effect of fragments and debris on security objects.

The studies of many scientists are devoted to the investigation of explosion damaging factors. Thus, in the publication [3], the estimation of the ASW action in an emergency explosion in the stock of ammunition is described, the main physical processes are described with the action of the ASW on surrounding objects, the basic parameters of the ASW are defined: excess pressure at the front of the ASW, impulse

of pressure at the compression phase, action of the ASW and a safe distance at shock wave action. Formulas and dependences obtained in the research can be adapted and used to study an explosion case, for example, a terrorist act.

In the work by Vadulina, Achyvakov and Sanimov [4], the main bases of human life insurance during the explosion of the pipeline are considered, the dependence of the conditional probability of human damage on the change in excess pressure of the shock wave of the explosion is studied. In the works [5]–[8], the influence of explosive lesions on the human organism is examined during technogenic catastrophes and terrorist acts.

The research by Chernozubenko, Kuprinenk and Bisik [9] provides the analysis of the damage factors on the human body after the explosion for the possibility of providing a complex system of personal protection. The distribution of injuries of body parts of military personnel during an explosion have been graphically depicted. The damage factors of the blow-ups of the explosive device have been considered, such as primary (fragments of an explosive device and a shock wave) and secondary factors (personnel fall from equipment, damage by buildings and structures, stress and heart attacks).

Study [10] helped establish the mechanogenesis of the impact of the damage factors of explosive devices on the human body. The results of the analysis showed that the main types of damage were injuries of the lower extremities, internal organs, and head.

Kryuchkova, Arzhavkina and Zhekalov in their research [11] presented the results of studying the dynamics of physical work ability and behavioral reactions of white rats at different intervals of the first day after the damage by the air shock wave of light and medium severity.

In the works by Luchko, Remez, Vorobiov, new types of EX were described [12]–[15]. The authors also compared different variants of charging pores and argued about the perspective use of these EX. However, the issue of the impact of air shock waves of new blended EX remains open.

3. NUMERICAL MODELLING

The goal of the research is the theoretical substantiation of the parameters of air shock waves during explosions of charges of traditional and new blended EX to predict their destructive effect on the environment.

To achieve the goal, the following objectives are set:

- to carry out mathematical modelling of the process of propagation of air shock waves during explosions and their interaction with natural-technogenic ecosystems;
- to establish the mathematical dependences of parameters of air shock waves on the type and mass of the explosive and the distance from the source in order to calculate their effect on living organisms.

An explosion of the spherical charge of EX in the air is considered. The motion of detonation products and air is described by a system of differential equations that determine the laws of conservation of the amount of motion, mass and impulse [2]:

$$\frac{\partial u}{\partial t}+u\frac{\partial u}{\partial r}+\frac{1}{\rho}\frac{\partial p}{\partial r}=0, \quad (1)$$

$$\frac{\partial \ln\rho}{\partial t}+u\frac{\partial \ln\rho}{\partial r}+\frac{\partial u}{\partial r}+\frac{Nu}{r}=0, \quad (2)$$

$$\frac{\partial(p/\rho^{\gamma})}{\partial t}+u\frac{\partial(p/\rho^{\gamma})}{\partial r}=0, \quad (3)$$

where r – coordinate, u – speed, p – pressure; t – moment of time; γ – isentrope index; ρ – density.

Expansion of detonation products takes place according to binomial isentropy [2]:

$$P=A\rho^{N}+B\rho^{\gamma+1}. \quad (4)$$

Constants in equation (2) characterise this type of EX. The initial conditions of this task are:

$$u=0,\ p=p_n,\ \rho=\rho_n \text{ at } 0\le r<r_0, \quad (5)$$

$$u=0,\ p=0,\ \rho=\rho_0 \text{ at } r_0\le r, \quad (6)$$

where r_0 – charge radius, p_n, ρ_n – pressure and density of detonation products in the explosion, ρ_0 – density of air.

The boundary conditions are as follows: 1) the condition of continuity of speed u and pressure on the moving contact boundary "products of detonation – air"; 2) the condition of "non-penetration" – the speed on the charge axis is zero. For the approximation of the system of differential equations (1)–(3) with the corresponding initial and boundary conditions, the method of finite differences was used based on the finite-difference scheme of the type "cross" [39] of the second order of accuracy in spatial and temporal coordinates.

To calculate the effect of traditional and new blended explosives on the shock wave parameters, the following EX are studied: trotyl, polymyx GR1/8 (74%)+KRUK2 (26%), compolite GS6, polymix GR4-T10 (Table 1).

Table 1

Parameters of Explosion of TNT and New Blended EX

No.	EX	Parameters						
		p_n, GPa	Q, KJ/kg	γ	ρ_0, kg/m^3	A	B·10^{-5}	N
1	Trotyl	9.8	4184	1.25	1600			3.12
2	Polymyx GR1/8	4.54	3355.7	1.242	1000	59.35	0.604	2.48
3	Compolite GS6	1.75	3919.7	1.235	852	7.671	1.638	2.24
4	Polymix GR4-T10	2.71	3864.4	1.245	872	5.67	1.279	2.73

As a result of the numerical solution to the problem, graphic functional dependences of the change of excess pressure on the distances of the spread path for different charge radii of different types of EX were obtained. For example, in Fig. 1 $r_0 = 0.2$ m.

As a result of the calculations, it is clear that the excess pressure of the air shock wave formed during the explosion of a traditional explosive substance – TNT – is much larger than during the explosion of new blended explosives. At a distance of the air-shock wave spread in 1 m in the explosion of charges with a radius of 0.1 m and 0.2 m, the excess pressure for TNT is by 2 times greater than for new blended EX. At a distance of 1.5 m and 2 m, the difference is reduced to 90 %–75 %. At a distance of 5 m from the epicenter of the explosion, the excess pressures are almost the same. This is due to the fact that in the near area of explosion, TNT has significantly larger parameters of the explosion (pressure, density, heat of radiation, etc.), but with an increase in the distance from the explosive cavity the waves formed by the explosion of TNT expire considerably more intensively than from blended EX because in the explosion of the charges of TNT the energy losses at the front of the shock wave are much higher.

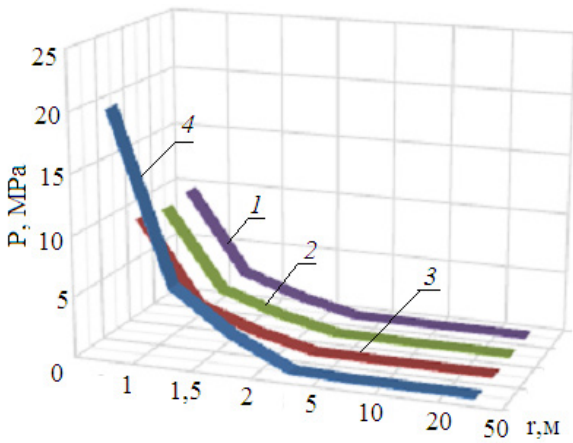

Fig. 1. Dependence of the change in excess pressure of the air shock wave on the explosion centre at $r_0 = 0.2$ m: 1 – polymix GR1/8; 2 – compolite; 3 – polymix GR4-T10; 4 – TNT.

From this we can conclude that in the distant zone of the explosion, the parameters of air shock waves are weakly dependent on the type of EX, and are determined by the mass of charge.

Thus, it can be stated that a traditional explosive substance, such as TNT, forms a stronger excess pressure during the explosion, and therefore the force of destruction of surrounding objects is higher than in new blended explosives. The application of the polymix GR4-T10, the compolite GS6 and the polymix GR1/8 (74 %) + KRUK2 (26 %) during blasting works is safer in terms of excess pressure formation.

After comparing the explosion of charges of traditional and new blended EX charges with excess pressure at the shock wave front, an impulse for the same explosives was calculated. As an example, Fig. 2 shows the dependence of the impulse on excess pressure during the explosion of charges of polymyx GR4-T10 with different radii.

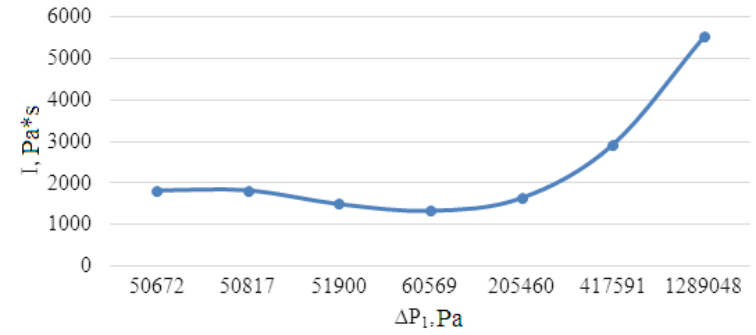

a)

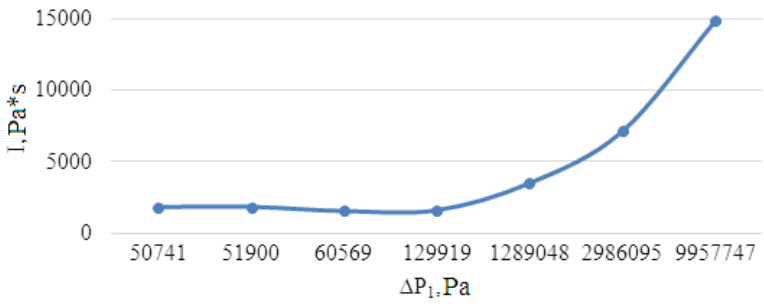

b)

Fig. 2. Dependence of the impulse from the excess pressure in the explosion of charges of polymix GR4-T10 with different radii: a) at r_0 = 0.1 m; b) r_0 = 0.2 m

As a result of calculations and graphic representation of the dependence of the impulse on excess pressure, it is evident that with an increase in excess pressure the impulse of the air shock wave increases. Impulse of the air shock wave formed during the explosion of a traditional explosive – TNT – is more by 40 % than during the explosion of new blended explosives for all investigated charge radii at a distance of 1 m from the epicenter of the explosion. At a distance of 1.5 m and 2 m, this difference is 30 % and 20 %, respectively. At a distance of 5 m, the value of the

impulse is almost the same for charges with radii of 0.1 m and 0.2 m, but for a charge with a radius of 1 m – at a distance from the epicenter of the explosion from 1.5 m to 20 m, the difference is 40 %, and from 20 m – 20 %.

Consequently, a traditional explosive substance, such as TNT, forms a stronger impulse during the explosion, and therefore the force of destruction of surrounding objects is higher than in new blended explosives. The application of the polymix GR4-T10, the compolite GS6 and the polymix GR1/8 (74 %) + KRUK2 (26 %) during blasting works is safer from the point of view of impulse formation.

Table 2 presents the results of calculations of the dependence of the degree of damage to people during the explosion of TNT and new blended EX on the distance of the spread of an explosive wave for different charge radii.

From Table 2, it can be concluded that the use of such a traditional explosive like TNT is more dangerous to human health than the use of new blended explosives, as, for example, the death of people as a result of direct exposure to ASW from the time of the explosion of EX with r_0 = 0.1 m at an excess pressure of 190 KPa for TNT will take place at a distance of 2.5–3 m, and during the explosion of new blended EX – at a distance of 3 m–3.5 m.

Table 2

The Degree of Damage to People in the Explosion of Different EX

Degree of damage	ΔP_l, *Pa*	Spread of an explosive wave, r_H, m (*)		
		r_0 = 0.1m	r_0 = 0.2m	r_0 = 1m
Death of people as a direct effect of ASW Death of people under the ruins of buildings Death of people as a result of smite from solid objects	190000	2.5-3 3-3.5	5-6 5.5-6.8	25-31,5 47-48
Serious damage as a result of ASW action Serious damage when the building collapses or the body moves by an explosive wave	69000-76000	4.5-6 4.7-7.8	9.5-10.5 7.3-8.5	49.5-50.5 more than 50
Serious damage as a result of eardrums and lungs under action of an explosive wave Defeat by fragments and ruins of the building	55000	8-9 10-11	16-16.5 more than 50	more than 50
Defeat by fragments and ruins of the building. Probability of rupture of drum chambers 10 %	24000	more than 50	more than 50	more than 50
Temporary loss of hearing or injuries as a result of secondary effects of an explosive wave (collapse of the building and body transference) Fatal or serious damage from direct exposure of an explosive wave is unlikely	16000	more than 50	more than 50	more than 50
Injuries associated with the destruction of glass and damage to the walls of the building	5900–8300	more than 50	more than 50	more than 50

* The numerator contains data for the TNT, in the denominator – for new compound substances.

In work [63] with the experimental data, the degree of contusions (DC) in dogs caused by the action of air shock waves was analyzed, which came with the following values of maximum and average pressure. At the same time, the authors proposed the use of parameter $P_{cp} = I_{yд} / t$, equal to the ratio of the specific impulse to the time of action of the ASW because the spread of experimental data is much smaller than for P_{max}. In order to assess the damage of people in the explosion of EX, in emergencies or terrorist acts, it is important to assess the likelihood of getting a damage from the ASW and the degree of contusion, and the most acceptable is the class of parametric laws of damage (PLD) using the Weibull-Gnedenko distribution. To solve this problem, the recalculation of the degree of concussion at certain parameters of air shock waves was performed in the research.

For practical application of theoretical results of the spread of ASW and their effects on environment, the method of calculating the safe parameters of the explosion was developed.

To construct the dependence of P_{cp} from the relative distance $\bar{r} = \sqrt[3]{m} / r$, calculations were carried out, for example, for TNT they are given in Table 3.

Table 3

Dependence of the Pressure on the Relative Distance for TNT

r, m	$\sqrt[3]{m} / r$			ΔP_{cp}, P_a		
	m=6.7kg	m=13.4kg	m=6702kg	m=6.7kg	m=13.4kg	m=6702kg
1	1.885	2.375	18.848	$2.6 \cdot 10^6$	$20.13 \cdot 10^6$	$2.5 \cdot 10^9$
1.5	1.26	1.58	10.57	$0.8 \cdot 10^6$	$6 \cdot 10^6$	$7.44 \cdot 10^8$
2	0.943	1.188	9.424	$0.36 \cdot 10^6$	$2.6 \cdot 10^6$	$3.14 \cdot 10^8$
5	0.38	0.48	3.77	$70.7 \cdot 10^3$	$211 \cdot 10^3$	$2 \cdot 10^7$
10	0.19	0.24	1.9	$53 \cdot 10^3$	$60.7 \cdot 10^3$	$2.56 \cdot 10^6$
20	0.095	0.12	0.95	$50.9 \cdot 10^3$	$53.2 \cdot 10^3$	$0.36 \cdot 10^6$

On the basis of the established dependences of excess pressure, specific impulse from the type and mass of EX, as well as the distance from the source of the explosion, a nomogram to determine the distances or masses of EX, safe for living organisms was built (Fig. 3): 1 – trotyl, 2 – polymix GR1/8 (74 %) + KRUK2 (26 %), 3 – the compolite GS6, 4 – the polymix GR4-T10. The following degrees of concussion are marked: 1 – light, 2 – medium, 3 – hard, 4 – difficult edge, 5 – death.

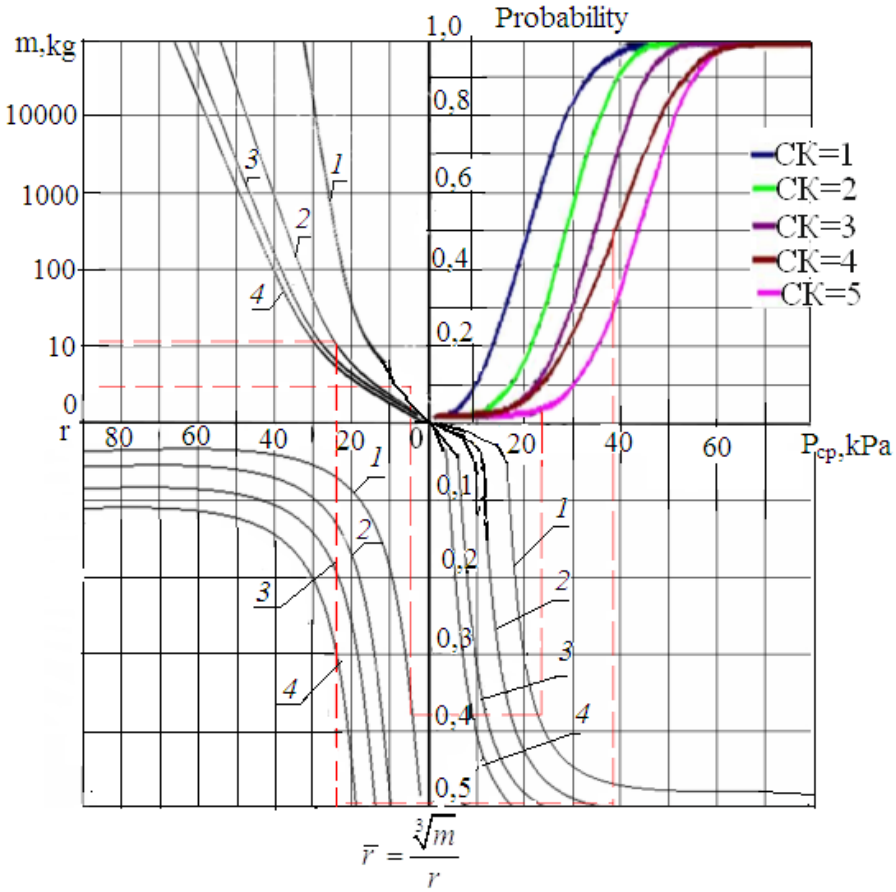

Fig. 3. Nomogram to determine the safe parameters of explosion of different EX for dogs, rabbits, pigs: 1 – trotyl, 2 – polymix GR1/8 (74 %) + KRUK2 (26 %), 3 – the compolite GS6, 4 – the polymix GR4-T10.

Figure 4 presents nomograms for determining the safe parameters of explosion for people in the explosion of charges of different types of EX. Numbering of curves in Fig. 4 corresponds to the numbering of Fig. 2.

4. RESULTS AND DISCUSSION

As it is known, the main parameters of the air shock wave, which determine its destructive and striking effect, are excess pressure, speed pressure, specific impulse of pressure and action time of the positive phase of the shock wave.

Today, new non-TNT blended EX, the technical and economic efficiency of which is proven, become a widespread practice. However, there is no theoretical substantiation of the environmental safety of the use of these EX and the interaction of airborne explosive waves during explosive operations with elements of ecosystems.

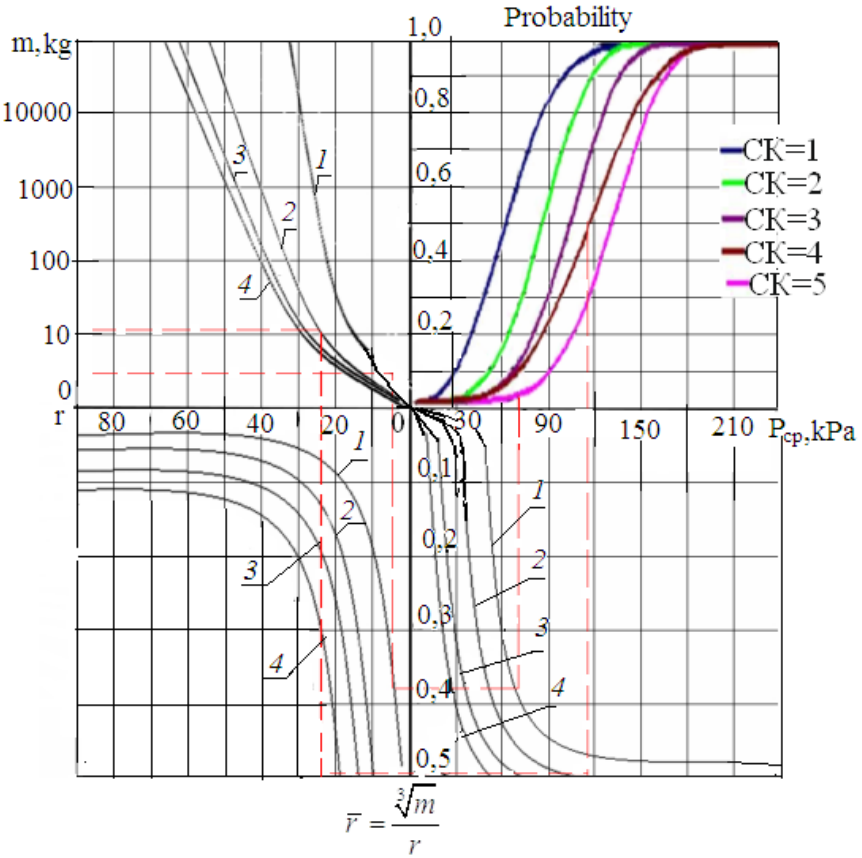

Fig. 4. Nomogram to determine the safe parameters of explosion of different EX for people:
1 – trotyl, 2 – polymix GR1/8 (74 %) + KRUK2 (26 %), 3 – the compolite GS6,
4 – the polymix GR4-T10.

On the basis of mathematical modelling, the research investigates the dependence of the change in parameters of air airborne explosive waves on the mass of charge of explosive at different distances from the epicenter of the explosion. For a charge weighting 10 kg, the following dependences for the ASW parameters are established, i.e., for the TNT: excess pressure $y = 9901.3x^{0.7034}$, pressure of the speed throng $y = 423.12x^{1.301}$, specific impulse $y = 0.63x^{0.6667}$, action time of the positive phase of the wave $y = 4.6171x^{0.1667}$; for the polymix GR4-T10: excess pressure $y = 7932.4x^{0.647}$, pressure of the speed throng $y = 250.87x^{1.2262}$; for the compolite GS6: excess pressure $y = 7932.4x^{0.647}$, pressure of the speed throng $y = 250.87x^{1.2262}$; for the polymix GR1/8 (74 %) + KRUK2 (26 %): excess pressure $y = 7457.5x^{0.636}$, pressure of the speed throng $y = 218.73x^{1.211}$.

For a charge weighting 50 kg, the following dependences for the ASW parameters are established, i.e., for the TNT: excess pressure $y=4\cdot10^{6}x^{-1.535}$, pressure of the speed throng $y = 5\cdot10^{7}x^{-3.005}$, specific impulse $y = 85.545x^{-1}$, action time of the positive phase of the wave $y = 2.8025x^{-0.5}$; for the polymix GR4-T10: excess pressure $y = 2\cdot10^{6}x^{-1.424}$, pressure of the speed throng $y = 1\cdot10^{7}x^{-2.803}$; for the compolite GS6: excess pressure $y = 2\cdot10^{6}x^{-1.426}$, pressure of the speed throng $y = 1\cdot10^{7}x^{-2.806}$; for the

polymix GR1/8 (74 %) + KRUK2 (26 %): excess pressure $y = 2 \cdot 10^6 x^{-1.407}$, pressure of the speed throng $y = 1 \cdot 10^7 x^{-2.772}$.

Based on the comparison of the calculated results and the degree of damage we have, the use of an explosive such as TNT is more dangerous to human health than the use of new blended explosives because, for example, the death of people as a result of direct influence of ASW in explosion of EX with 0.1 m at an excess pressure of 190 KPa for TNT takes place at a distance of 2.5 m–3 m, while during the exploion of new blended EX – at a distance of 3 m–3.5 m.

Based on the established dependences of excess pressure, specific impulse from the type and mass of charge of EX, as well as the distance from the epicenter of the explosion, an engineering method was developed for calculating the dangerous parameters of the explosion on the environment.

5. CONCLUSIONS

1. The effective calculation method based on numerical simulation of the explosion of spherical charges of traditional and new explosives in the air has been developed, which allows obtaining the parameters of airborne shock waves, depending on time, distance, mass of charge and type of EX.
2. Based on the mathematical modelling of the spread of airborne shock waves and their interaction with natural-technogenic environment, the influence of traditional and new blended explosives on the parameters of ASW has been studied. As a result of numerical calculations, it has been established that during the explosion of charges of traditional EX (trotyl), a stronger excess pressure (by an average 85 %) than in the new blended EX is formed. Consequently, the use of the polymix GR4-T10, compolite GS6 and polymix GR1/8 (74 %) + KRUK2 (26 %) during blasting works is safer in terms of excess pressure formation.
3. The functional (degree) dependences of excess pressure on the distance of the source of the explosion and the charge and impulse mass on the excess pressure and the charge radius for different types of EX have been determined.
4. It has been established that with an increase in excess pressure, the impulse of the airborne shock wave increases. When using TNT, a specific impulse is generated, which is much stronger (by 40 %) than that of blasting new blended explosives.
5. It has been established that the destructive and damaging effect of the explosion charge of TNT is much greater than of the new blended EX. The safe distance from the source of the explosion of such charges increases by 25 %–50 %.
6. The engineering methodology has been developed for calculating the dangerous parameters of the explosion on the environment based on the established dependences of excess pressure, specific impulse on the type and mass of charge of EX, as well as the distance from the epicenter of the explosion.

REFERENCES

1. Sadovsky, M.A. (1952). The *Mechanical Action of Air Shock Waves of Explosion According to Experimental Studies: Physics of Explosion*. Moscow: Publishing of Academy of Sciences of the USSR.
2. Baum, F.A., Orlenko, L.P., Stanyukovich, K.P., Chelyshev, V.P., & Schechter, B.I. (1975). *Physics of the Explosion*. Moscow: Science.
3. Sidorenko, V.L., & Azarov, S.I. (2008). Calculation of the effects of explosive shock waves on a person during an explosion in the stock of ammunition. *Systems of Armament and Military Equipment*, *1*, 70–73.
4. Vadulina, N.V., Achivakova, L.R., Salimov, A.O., Abdrakhmanova, K.N., & Abdullin R.S. (2017). Insuring safety pneumatest of the pipeline. *Oil and Gas Business*, *4*, 109–124. DOI: http://dx.doi.org/10.17122/ogbus-2017-4-109-124
5. Minnullin, I.P., Fomin, N.F., & Nechaev, E.A. (2010). Mine-explosive defeats – the global problem of humanity. *Medicine of Catastrophes*, *2*, 34–36.
6. Shapovalov, V.M., & Samokhvalov, I.M. (2012). Explosive injuries due to man-made disasters and terrorist acts. *War-Medical Journal*, *1*, 25–33.
7. Kaptsov, V.A., Kulbacinskiy, V.V., Bazaz'yan, A.G., Romanov, V.V., & Semenchukov, A.V. (2010). Probable injuries and specifics of preparedness planning for and management of acts of terrorism on railways. *Medicine of Catastrophes*, *1*, 15–18.
8. Shapovalov, V.M., Samokhvalov, I.M., & Lytaev, S.A. (2012). Amazing factors, mechano-pathogenesis, clinical manifestations of explosive damage of peacetime. *Quality Management in the Sphere of Health Care and Social Development*, *3*, 46–51.
9. Chernozubenko A.V., Kuprinenko, A.N., & Bisyk, S.P. (2014). Study of damaging factors sap mine explosive devices on the human body. *Systems of Armament and Military Equipment*, *2*, 39–44.
10. Ivanitski, A., & Petriko, H. (2014). Assessment of consequences of impact of emergency explosion of fuel-air mixture on a person. *Bulletin of the Command-Engineering Institute of the Ministry of Emergencies of the Republic of Belarus*, *1*(19), 67–72.
11. Kriuchkova, A.S., Arzhavkina, L.G., Zhekalov, A.N., Protasov, O.V., & Chernyavskiy, E.A. (2015). Influence of blast wind injury of minor and medium severity on physical efficiency and behavioral reactions in animals. *Herald of the Russian Military Medical Academy*, *1*(49), 169–172.
12. Luchko, I.A., Remez, N.S., & Luchko, A.I. (2010). Wave processes in soil massifs during explosions of new blended explosives. *Bulletin of NTUU "KPI". Series "Mining"*, *19*, 24–25.
13. Luchko, I.A., Remez, N.S., & Luchko, A.I. (2011). Mathematical modeling of the explosion in soils and rocks. Kyiv: NTUU "KPI".
14. Remez, N.S., Luchko, I.A., & Luchko, A.I. (2006). Efficiency of application of new non-destructive explosives at consolidation of soil bases. *SRI of Building Constructions*, *64*, 296–301.
15. Vorobiov, V.D., & Tverda, O.Y. (2012). Justification of the criterion for selecting a safe and effective type of explosives in mass explosions in quarries. *Problems of Labor Protection in Ukraine*, *22*, 56–64.
16. Remez, N., Dychko, A., Kraychuk, S., Ostapchuk, N., & Yevtieieva, L. (2018). Simulation of seismic explosion waves with underground pipe interaction. *Journal of Physics and Engineering*, *3*, 27–33. DOI: http://dx.doi.org/10.2478/lpts-2018-0011

17. Remez, N., Dychko, A., & Yevtieieva, L. (2018). Stress-deformed state of soil at the explosion of cylindrical charge of new industrial mixed explosives. *Development of Scientific Foundations of Resource-Saving Technologies of Mineral Mining and Processing* (pp. 105–125). Sofia: Publishing House St.Ivan Rilski.
18. Remez, N., Dychko, A., Kraychuk, S., & Ostapchuk, N. (2018). Interaction of seismicexplosive waves with underground and surface structures. *Resources and Resource-Saving Technologies in Mineral Mining and Processing* (pp. 291–310). Petroşani, Romania: UNIVERSITAS Publishing.
19. Isayenko, V.M., Vovk, O.O., Zaychenko, S.V., Remez N.S., & Vovk, O.O. (2018). *Methods of Forecasting and Monitoring of Technogenic Dynamic Processes in the Extraterritorial Territories*. Kyiv: NAU.
20. Guselskikov, Y.O., Vylokhin, S.A., & Ponikarov, S.I. (2014). Study of effective parameters of an air shock wave. *Bulletin of the Kazan Technological University*, *9*, 81–83.

SPRĀDZIENBĪSTAMU MAISĪJUMU SPRĀDZIENA IETEKMES MODELĒŠANA UZ VIDI

N. Remezs, A. Dičko, J. Besarabets, S. Kraičuks,
N. Ostapčuks, L. Jevtejeva

K o p s a v i l k u m s

Rakstā aprakstīta tradicionālo (trotils) un jauno sajaukto sprāgstvielu lādiņu eksplozijas modelēšana: polimiks GR1/8 (74 %) + KRUK2 (26 %), kompolīts GS6, polimiks GR4-T10. Pētījuma rezultātā tika konstatēts, ka, izmantojot TNT, veidojas īpašs impulss, kas ir par 40 % lielāks nekā jaunu jauktu sprāgstvielu sprādziens, un drošais attālums no šādu sprāgstvielu sprādziena avota tiek palielināts par 25% – 50%. Pamatojoties uz konstatētajām pārspiediena atkarībām, īpašo impulsu uz lādiņa veidu un masu, kā arī attālumu no sprādziena epicentra tika izstrādāta inženiertehniskā metode, lai aprēķinātu sprādzienbīstamu parametru ietekmi uz vidi.

12.02.2019.

sciendo

LATVIAN JOURNAL OF PHYSICS
AND TECHNICAL SCIENCES
2019, N 3

DOI: 10.2478/lpts-2019-0019

ENGINEERING AND TECHNOLOGY

LOW-COST L-BAND RECEIVING SYSTEM FRONT-END FOR IRBENE RT-32 CASSEGRAIN RADIO TELESCOPE

M. Bleiders*, A. Berzins, N. Jekabsons, K. Skirmante, Vl. Bezrukovs
Engineering Research Institute "Ventspils International Radio Astronomy Center",
Ventspils University College, Inzenieru Str. 101, Ventspils, LV-3601, LATVIA
*e-mail: marcis.bleiders@venta.lv

Irbene RT-32 radio telescope is one of the main instruments operated by Ventspils International Radio Astronomy Center (VIRAC), which is used for participation in VLBI and single-dish mode observations, including European VLBI Network (EVN) and other astronomy projects such as recently started research on small bodies of solar system, which involves weak spectral line detection at L-band. Since start of the operation as a radio telescope, single C-X band receiver has been available at RT-32, but regular demand for L-band frequencies has been received due to its importance in spectral line science. In case of RT-32 geometry, optimum dimensions of L-band feed antenna system are inconveniently large and its installation without significant feed cone rebuilding is complicated. While work is currently ongoing to redesign the feed cone for multiple receiver support and to develop high performance L-band feed system, temporal, compact and low-cost receiver has been built and installed laterally to secondary focus, which in sense of performance and functionality has been proven to be appropriate for most of the current needs. Receiver is based on small parabolic reflector allowing one to use a compact dual circular polarized horn antenna, which together with a Cassegrain antenna forms a three-mirror system. Front-end is uncooled that allows reducing operational and maintenance costs, while still providing acceptable noise performance. Practical tests show average overall sensitivity of 750 Jy at 1650 MHz in terms of system effective flux density (*SEFD*). The paper describes the development of the receiver and presents the main results of performance characterization obtained at Irbene RT-32.

Keywords: *feed antenna, radio telescope, receiver*

1. INTRODUCTION

RT-32 originally was built as a satellite communications station. Only in recent years it has been refurbished to function as a radio telescope. Its secondary focus vertex room is intended for a single receiver feed system and currently a

cryogenic C-X band receiver is installed there. There were attempts to implement L-band receivers in existing RT-32 system based on a helical antenna array as a feed antenna [1], [2], but due to specific application of satellite signal reception, its performance specification was less constrained; as a result, sensitivity of these designs were not sufficient for astronomy involving natural sources. In addition, due to a feed solution, only a single polarization channel was available and manual installation of receiver before observation was required which increased maintenance cost, decreased frequency band agility, and complicated the calibration. To deal with these issues, a receiving system was redesigned, by employing a compact feed antenna permanently installed at secondary focus with lateral offset, uncooled low noise amplifiers and improved frequency conversion and control unit. The following sections of the paper describe the design process of the above-mentioned subsystems and summarise the main results of performance evaluation.

2. THE REQUIRED DIMENSIONS OF FEED ANTENNA

In case of RT-32 geometry, its Cassegrain ratio of focal length to diameter at secondary focus is $f/D = 2.7$, which translates to a secondary mirror subtended angle of $\theta = 21^{\circ}$. As an initial design specification, a rule-of-thumb required an illumination pattern edge taper of 10 to 13 dB. Design frequency is set to 1650 MHz, which is at the centre of frequency band usually observed by EVN. To obtain an idea of necessary optimum dimensions of feed antenna, first, we calculate ideal case corrugated feed horn dimensions by approximating the telescope as a quasi-optical system where feed horn must generate appropriate a Gaussian beam waist at focal position. Radius of beam waist can be calculated in terms of illuminated mirror effective ratio f/D and required edge taper [3, 6.68b]:

$$W_0 = 0.216\sqrt{|T(dB)|}\frac{f}{D}\lambda\,. \tag{1}$$

T is edge taper in dB. In case of RT-32, $W_0 = 0.34$ m is obtained at 1650 MHz and edge taper of 10 dB. For practical horn, a quadratic phase error of between the centre and edge of the aperture must be finite and here a phase error of $\beta = 1.26$ rad (0.2λ) is assumed. This allows finding corrugated feed horn aperture radius and slant length which maximizes coupling to a fundamental Gaussian beam mode [3], [4]:

$$a = W_0\frac{\sqrt{1+0.172\beta^2}}{0.644}\,, \tag{2}$$

$$L = \frac{\pi a^2}{\lambda\beta}\,. \tag{3}$$

Using (2) and (3), dimensions of aperture diameter and slant length of the hypothetical corrugated horn can be found: $D_\alpha = 2\alpha \approx 1.17$ m and $L \approx 4.7$ m, respectively. It is the large length, which is currently practically inconvenient in case of RT-32, so as a temporal solution, feed aperture is approximated by replacing the full-size horn with the third focusing reflector to reduce the final beam waist, thus allowing one to reduce dimensions of the required feed significantly. Similar approach has been reported in [5]. Standard size parabolic reflector with $D = 1.2$ m and ratio $f/D = 0.4$ (subtended angle $\theta = 128^\circ$) is used, which matches good with the previously calculated required aperture diameter D_α.

3. FEED HORN FOR ILLUMINATING THE THIRD REFLECTOR

Feed horn design was adapted from [6] and scaled to 1650 MHz. This horn consists of a single mode circular waveguide and /4 choke ring to suppress the sidelobes while its relatively small size reduces reflector blockage. Dual circular polarizations are obtained using a septum polarizer, which also serves to separate orthogonal modes. Before manufacturing, the feed horn was modelled and optimized for the best return loss with practical metal part thicknesses using CST MWO. Waveguide to coaxial transitions was also included in simulation. Simulated far fields are shown in Fig. 1, while Fig. 5 demonstrates simulated and measured S parameters.

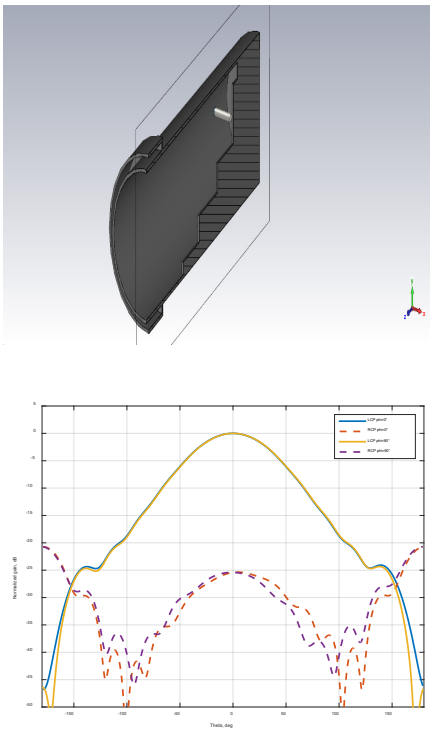

Fig. 1. (Left) Cutting plane of 3D model of feed horn in CST. (Right) Simulated far field RCP and LCP beam patterns at Phi cuts of 0º and 90º.

The main dimensions of final optimized feed horn at 1650 MHz are the following: D_α = 132 mm, L = 393 mm, Thickness of septum: 5 mm. As follows from Fig. 1, the same beam width at both Phi planes with a cross-polar level of 25 dB is obtained. Amplitude taper at beam angle of θ = 128º is ≈ 9.4 dB.

4. MODELLING OF REFLECTOR SYSTEM

As the first step, the system consisting of feed horn and 1.2 m parabolic reflector is analysed in CST and the obtained far-field beam patterns are shown in Fig. 2. Feed support metal tripod was also included in simulation. Unfortunately, blocked, electrically small aperture gives rise to relatively large sidelobes, which are non-symmetric due to feed supports. Offset reflector would reduce aperture blockage, but at the cost of increased overall dimensions. Cross-polarization level of feed horn antenna is preserved relatively well. Amplitude taper of the obtained pattern at RT-32 secondary mirror subtended angle of 21º is about 17 dB, which is larger (beam is narrower) than predicted when radiating aperture is corrugated horn with the same diameter.

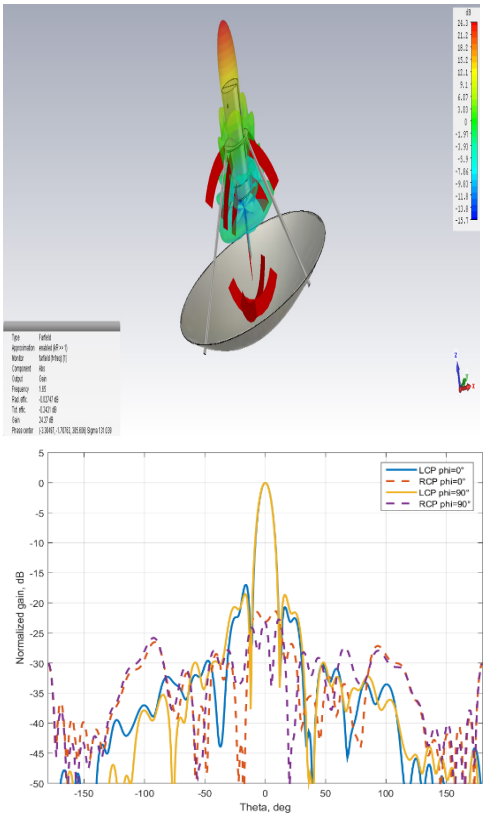

Fig. 2. (Left) 3D model of composite feed – 1.2 m third reflector and compact horn. Red area shows the position of far-field phase centre of the whole structure. (Right) Simulated far-field RCP and LCP beam patterns at Phi cuts of 0º and 90º.

Next, simple modelling of overall performance was performed using physical optics code based on [7]. Ideally aligned and appropriately meshed RT-32 Cassegrain reflector surfaces were assumed without considering the influence of the secondary mirror support leg. Far-field pattern shown in Fig. 2 was used as an illuminating point source – although distance between the source point and the first reflector is smaller than Fraunhofer distance of composite feed, results should still give a rough estimate of overall performance. Resulting boresight region beam patterns with composite feed offset and orientation angle relative to centre axis at secondary focus of 1 m and 8º, respectively, are shown in Fig. 3.

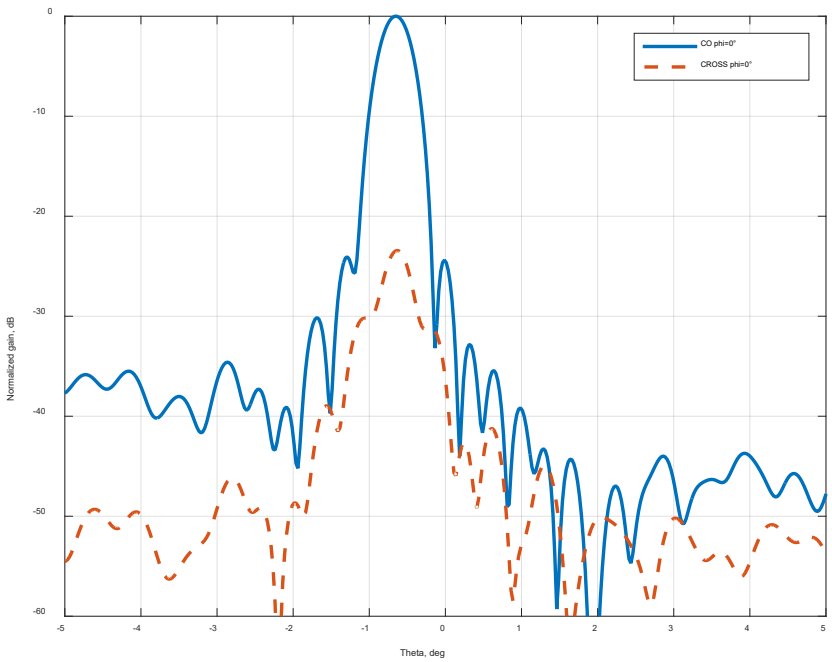

Fig. 3. Physical optics result of overall RT-32 co-polar and cross-polar beam pattern with a laterally shifted composite feed antenna. Pattern cut angle matches with lateral shift plane.

Maximum directivity of 52.3 dBi is calculated, which corresponds to aperture efficiency e_P = 0.55. As mentioned previously, an ideal reflector system was assumed. In the real world, efficiency would be degraded due to additional factors. It is estimated from photogrammetric measurements that RMS error of RT-32 primary surface is ≈4 mm, which translates to surface efficiency e_S = 0.9 at 1650 MHz according to Ruze. It is known from beam pattern measurements at C-band that the secondary mirror of RT-32 is misaligned – the assumed degradation at L-band is e_M = 0.9. Additional factor e_R = 0.9 is assumed due to secondary mirror support leg diffraction and imperfections of practical implementation. This would result in expected overall aperture efficiency not more than $e_A \approx e_P e_S e_M e_R$ = 40 %. Physical optics result also shows the main beam offset angle of -0.66º, which is opposite to lateral shift direction. The predicted cross-polarization level is 23 dB.

5. FEED ANTENNA INSTALLATION AT RT-32

Composite feed antenna was built and installed at RT-32 secondary focus with phase centre lateral offset of 1 m and angle of 8º as shown in Fig. 4. Before installation, S parameters of feed horn separately were measured with waveguide opening facing clear sky. Attempt was made to experimentally trim length of coaxial to waveguide interface monopole antennas to further optimize return loss, but no significant improvement was observed relative to dimensions predicted by CST. Measurement results show return loss better than 15 dB within the frequency range from 1450 to 1720 MHz (see Fig. 5). The measured port-to-port isolation is ≈18 dB at 1650 MHz.

Fig. 4. L-band feed antenna installed at RT-32 with offset from secondary focus.

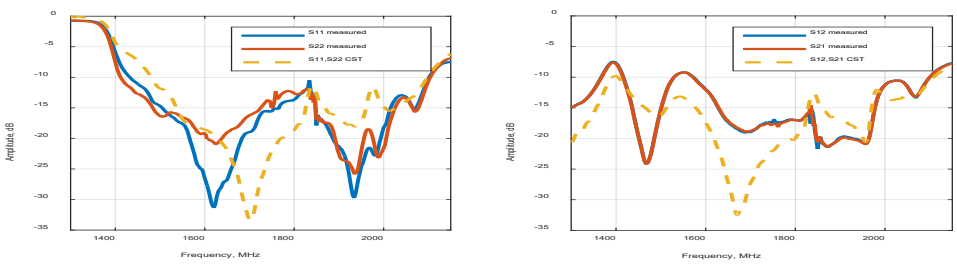

Fig. 5. The measured and predicted S parameters of feed horn. (Left) Return loss feed horn ports. (Right) Isolation between ports.

6. RECEIVER FRONT-END

Receiver front-end consists of two-channel low noise amplifiers (LNA), which are uncooled. LNAs are two-stage design optimized for the lowest noise figure at 1650 MHz. LNAs employ of-the-shelf MMIC device Skyworks SKY67151 for the first stage, and Mini-Circuits PGA103+ for the second stage. Input of LNAs contains microstrip directional couplers for calibration noise injection. While amplifiers are operated in the unregulated ambient environment, a calibration noise

source is positioned at the temperature regulated vertex room. Noise signal is fed via a separate coaxial cable through Wilkinson power divider to directional coupler inputs. Power supply voltage for amplifiers are provided through signal cables with the help of built-in bias-T circuits. To reduce degradation of noise temperature, short RG401 semi-rigid cables are used for connection between inputs of amplifiers and feed horn ports. Noise temperature of ≈30 K and gain of 32 dB was measured at 1650 MHz using Agilent 346A noise source. Results are shown in Fig. 7. Noticeable negative gain slope is equalized at intermediate frequency stages.

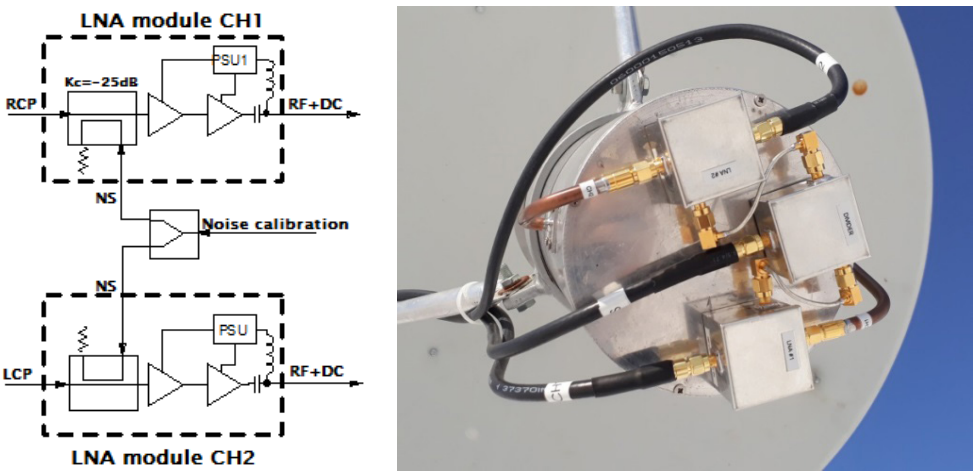

Fig. 6. Block diagram of receiver front-end and practical implementation. Amplifiers and calibration noise divider are positioned above the feed horn.

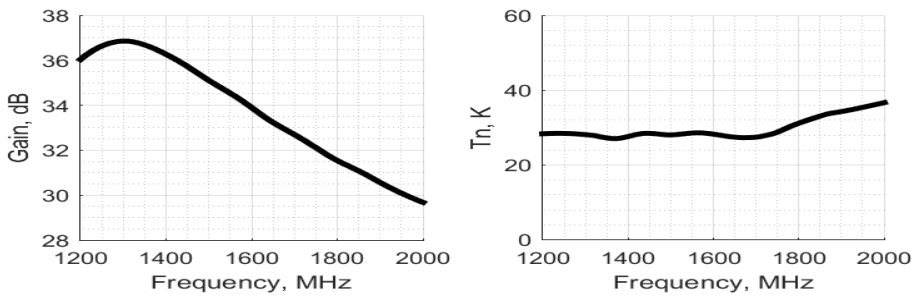

Fig. 7. Measured gain (left) and noise temperature (right) of L-band low noise amplifier. Measurement includes microstrip directional coupler at the amplifier input.

7. TELESCOPE SENSITIVITY

Sensitivity was evaluated in terms of system effective flux density (*SEFD*) by observing astronomical calibrator sources 3C123, 3C286 and 3C196 at various

antenna elevation positions. Standard "ON-OFF" procedure using frequency selective total power back-end was employed and *SEFD* calculated using (4):

$$SEFD = S_f \frac{P_{off}}{P_{on} - P_{off}} . \quad (4)$$

S_f is source flux density and T_{on}, T_{off} are total power values with beam pointing on and off source, respectively. Before *SEFD* measurement, beam pointing offsets were characterised and compensated by applying a pointing model, which was integrated in VLBI Field System software package. Weather conditions during measurement were excellent with clear sky and no wind. Result of measurement is showed in Fig. 8. As it can be seen, *SEFD* is 700 to 800 Jy within the typical operating elevation range between 20º and 60º.

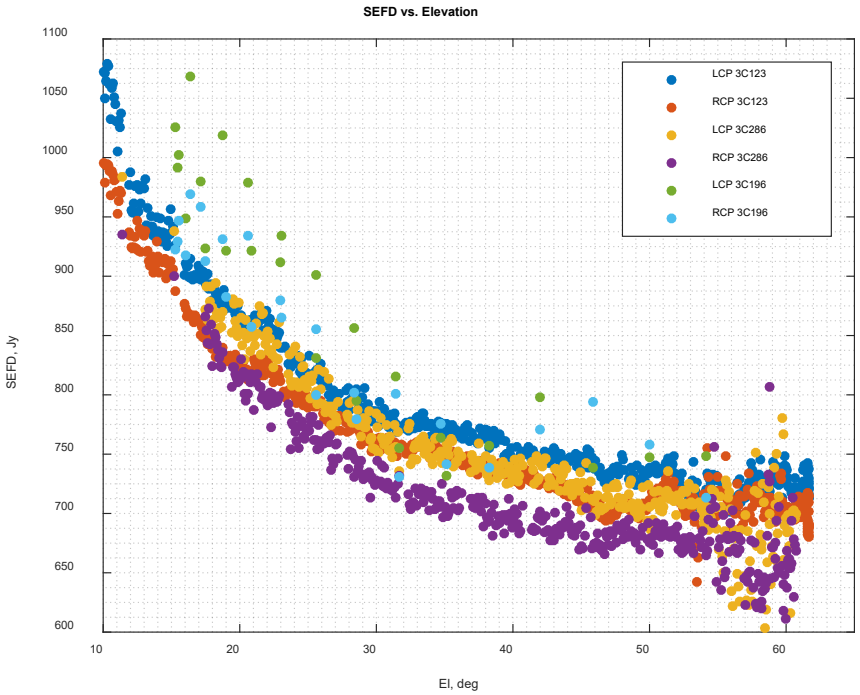

Fig. 8. Measured *SEFD* vs. elevation of RT-32 at 1650 MHz. Date of measurement: 6 April 2019.

SEFD is obtained by direct measurement and contains information about both the aperture efficiency and system noise temperature T_{sys}. To get an idea of actual aperture efficiency, absolute value of T_{sys} must be known. T_{sys} dependence on elevation was measured during *SEFD* measurement session and assuming injected calibration noise power was stable during relatively short measurement, relative characteristic shape of the measured T_{sys} curve should be accurate. To verify and compare absolute values of T_{sys} data, antenna noise temperature T_a was modelled using software described in [8], which rotates and integrates the antenna radiation

pattern in the elevation dependant noise environment. Full theta range radiation pattern version of Fig. 3 was used. Resulting T_{sys} is a sum of antenna and measured receiver noise temperatures ($T_n \approx 30$ K) and is shown in Fig. 9. Small correction to laboratory estimated injected calibration noise values used in T_{sys} measurements were applied using a simple constant scaling factor so that an absolute value of measured T_{sys} for both channels matches the theoretic curve. No correction to curve shape was applied as it already matched quite closely to the theoretic one. Obtained T_{sys} data together with *SEFD* measurements were used to calculate antenna aperture efficiency using (5):

$$e_A = 2k\frac{T_{sys}}{A_{phys}SEFD}10^{26}. \quad (5)$$

A_{phys} is a physical area of antenna, and k is Boltzmann constant. Resulting aperture efficiency is shown in left panel of Fig. 9. The obtained value of ≈ 26 % is 10 % less than the estimated one from physical optics simulation. Reason for this could be underestimated RT-32 surface and secondary mirror alignment efficiency factors or absolute values of T_{sys}. It should be mentioned that no influence of central C-band feed horn structure proximity (see Fig. 4) was modelled and should be investigated in future.

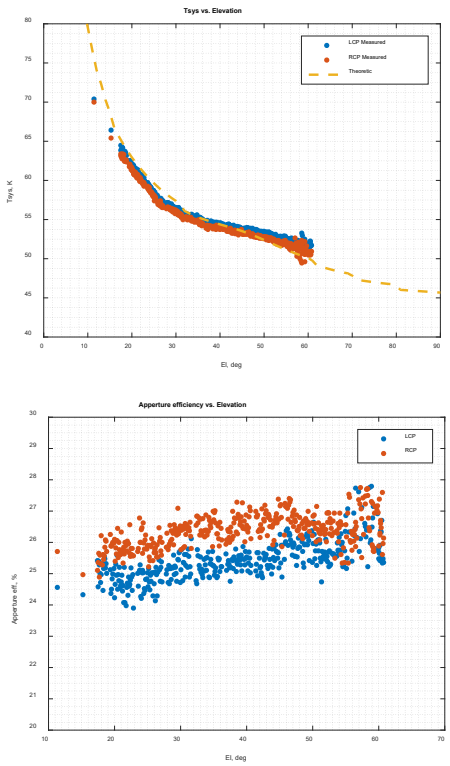

Fig. 9. (Left) The simulated and measured system noise temperature at 1650 MHz. (Right) The estimated aperture efficiency using data of Fig. 8 , Fig. 9 and (5). Data points were obtained from 3C286 calibrator observations.

8. THE FIRST OBSERVATION TESTS

Multiple astronomical observations were carried to test the receiver in single antenna and VLBI modes. Figure 10 shows the example of spectral line result obtained during single antenna mode tests. FFT spectrometer was used as registration backend in the frequency switching mode with spectral resolution of 0.38 KHz and integration time 80 seconds. Figure 11 highlights the result of EVN fringe test experiment FR057 at L-band. The obtained fringe amplitudes are comparable to other equivalent size antennas. Both results show acceptable isolation of cross-polarized channels.

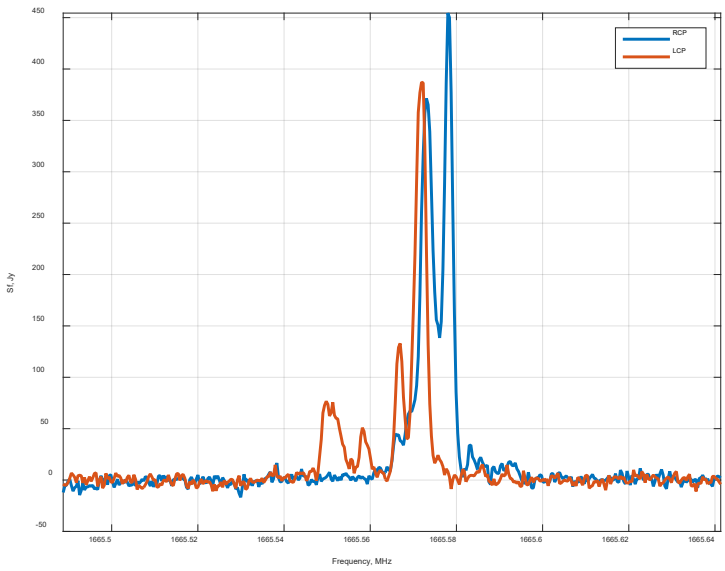

Fig. 10. Single antenna observation test result – spectral line towards W3(OH) at 1665 MHz. Total integration time: 80 s. Date of observation: 20 March 2019.

Vex file -- Integration time: 2s -- Start of the integration: 2019y023d14h20m00s0ms

FR057	Auto correlations						Cross correlations				
	Ef	Hh	Ir	O8	On	Tr	Ef-Hh	Ef-Ir	Ef-O8	Ef-On	Ef-Tr
1634.49MHz, LSB, Rcp-Rcp	1	1	1	1	1	1	276.2 A P offset: 0	634.8 A P offset: 0	895.6 A P offset: 3	838.4 A P offset: -1	1117 A P offset: 4
1634.49MHz, LSB, Rcp-Lcp	Cross hands						29.38 A P offset: 0	88.78 A P offset: 0	14.24 A P offset: 3	15.47 A P offset: 0	65.11 A P offset: 4
1634.49MHz, LSB, Lcp-Lcp	9	9	9	9	9	5	300.8 A P offset: 0	656.5 A P offset: 0	1062 A P offset: 3	870 A P offset: -1	776 A P offset: 4
1634.49MHz, LSB, Lcp-Rcp	Cross hands						15.92 A P offset: 0	149.9 A P offset: 0	60.64 A P offset: 3	65.15 A P offset: -1	187.5 A P offset: 4
1634.49MHz, USB, Rcp-Rcp	1	1	1	1	1	1	284.5 A P offset: 0	666 A P offset: 0	969.7 A P offset: -3	935 A P offset: 1	1070 A P offset: -4
1634.49MHz, USB, Rcp-Lcp	Cross hands						26.79 A P offset: 0	96.2 A P offset: 0	17.22 A P offset: -3	14.03 A P offset: 0	52.01 A P offset: -4
1634.49MHz, USB, Lcp-Lcp	9	9	9	9	9	5	260.8 A P offset: 0	628 A P offset: 0	1192 A P offset: -3	986 A P offset: 1	805 A P offset: -4
1634.49MHz, USB, Lcp-Rcp	Cross hands						13.58 A P offset: 0	134.4 A P offset: 0	67.9 A P offset: -3	68.6 A P offset: 1	215.2 A P offset: -4
1650.49MHz, LSB, Rcp-Rcp	2	2	2	2	2	2	297.5 A P offset: 0	654.2 A P offset: 0	1077 A P offset: 3	966.2 A P offset: -1	1070 A P offset: 4
1650.49MHz, LSB, Rcp-Lcp	Cross hands						23.99 A P offset: 0	79.23 A P offset: 0	16.69 A P offset: 3	11.53 A P offset: 0	56.11 A P offset: 4
1650.49MHz, LSB, Lcp-Lcp	10	10	10	10	10	6	249.2 A P offset: 0	657.1 A P offset: 0	1228 A P offset: 3	945.3 A P offset: -1	862.8 A P offset: 4

Fig. 11. First VLBI fringes using presented low-cost L-band receiver in EVN test observation FR057. Irbene RT-32 telescope designator is 'Ir'.

9. CONCLUSIONS

Low-cost L-band receiving system front-end intended for Irbene RT-32 Cassegrain radio telescope has been presented in the paper. Use of the third reflector significantly reduces feed antenna dimensions, hence, cost and complexly of manufacturing. Permanent installation at offset position reduces maintenance and frequency band switch-over time. Downside of this solution is reduced aperture efficiency due to diffraction losses of electrically small reflector and loss due to blocked aperture. In terms of system effective flux density, combined with uncooled low noise amplifiers, overall estimated telescope sensitivity is 700 to 800 Jy within usual elevation range, which corresponds to system noise temperature and aperture efficiency of ≈55 K and ≈26 %, respectively. The obtained sensitivity is average and could be improved 3 to 4 times if the appropriate full-size feed horn and cryogenic amplifiers are used, which already has been planned within ongoing RT-32 vertex room redesign project. Nevertheless, it has been proven by actual observations that performance of the presented system is sufficient to be useful as a temporal L-band receiver in various astronomy projects currently ongoing at VIRAC, including participation in EVN and observing relatively bright spectral lines in a single antenna mode.

ACKNOWLEDGEMENTS

The research has been funded by the Latvian Council of Science, project "Complex Investigations of the Small Bodies in the Solar System", No. lzp-2018/1-0401.

REFERENCES

1. Trokss, J., Lesins, A., Gaigals, G., Nechaeva, M., & Bezrukovs, Vl. (2013). Receiving system for ionosphere research. *Latvian Journal of Physics and Technical Sciences*, *49*(6), 13-17. DOI: 10.2478/v10047-012-0038-9
2. Bleiders, M., & Trokss, J. (2016). Development of receiver system for radio-astronomical observations at L band. *Space Research Review*, *4*, 77–84. ISBN 978-9984-648-64-4
3. Goldsmith, P. F. (1998). Quasioptical Systems: Gaussian Beam Quasioptical Propogation and Applications. *Wiley-IEEE Press*. ISBN: 978-0-7803-3439-7
4. Wylde, R. J. (1984). Millimetre-wave Gaussian beam-mode optics and corrugated feed horns. *IEE Proceedings, Part H - Microwaves, Optics and Antennas, 131*, 258–262. DOI: 10.1049/ip-h-1.1984.0053
5. Galuscak, R., Watanabe, M., Hazdra, P., Takeda, S., Seki, K., Prochazka, M., & Uchiyama, Y. (2008). Design of primary feeds for 32m KDDI antenna system IBA-4 in Cassegrain configuration. *Radio Engineering, 17(1)*. 20-27.
6. Galuscak, R., Hazdra, P. (2007). Prime-focus circular waveguide feed with septum polarization transformer, *DUBUS* 36(1), 8-32. ISSN: 1438-3705
7. Arias-Acuña, M., García-Pino, A., & Rubiños-López, O. (2013). Fast far field computation of single and dual reflector antennas. *Journal of Engineering, 2013*. DOI: 10.1155/2013/140254

8. Galuscak, R., Galuščáková, P., Mazanek, M., Hazdra, P., & Macas, M. (2009). Antenna Noise Temperature Calculator, *DUBUS* 3/2009. ISSN: 1438-3705

L DIAPAZONA UZTVEROŠĀS SISTĒMAS IEEJAS TRAKTS IRBENES RT-32 RADIOTELESKOPAM

M. Bleiders, A. Bērziņš, N. Jēkabsons,
K. Šķirmante, V. Bezrukovs

Kopsavilkums

Irbenes RT-32 radioteleskops ir viens no galvenajiem Ventspils Starptautiskā Centra (VSRC) instrumentiem, kas tiek izmantots VLBI un vienas antenas režīma novērojumos, tai skaitā dalībai Eiropas VLBI tīklā (EVN) un citos astronomijas projektos, piemēram, nesen uzsāktajā projektā "Kompleksie Saules sistēmas mazo ķermeņu pētījumi", kas saistās ar vāju spektrālo radiolīniju uztveršanu L diapazonā. Kopš darbības uzsākšanas, RT-32 ir pieejams C-X diapazona uztvērējs, bet regulāri tiek saņemts pieprasījums pēc novērojumiem L diapazona frekvencēs. RT-32 ģeometrijas gadījumā, optimālas veiktspējas iegūšanai L diapazonā ir nepieciešams ļoti liela izmēra apstarotājs, kura instalācija bez ievērojamas sekundārā fokusa konusa pārbūves ir sarežģīta. Kamēr šī pārbūve tiek veikta un tiek projektēts augstas veiktspējas apstarotājs, kā pagaidu risinājums ir izstrādāta kompakta uztverošā sistēma, kas ar sānisku nobīdi ir instalēta sekundārajā fokusā. Ņemto vērā ierobežoto izstrādes un izgatavošanas budžetu, iegūtā uztvērēja veiktspējā ir pietiekama lielai daļai šī brīža VSRC vajadzībām. Uztvērējs sastāv no maza izmēra paraboliskās antenas, kas ļauj izmantot kompaktu apstarotāju ar diviem cirkulāri polarizētiem kanāliem, tādējādi kopumā veidojot trīs spoguļu sistēmu. Ieejas trakta priekš pastiprinātāji netiek dzesēti, kas ļauj samazināt izgatavošanas un uzturēšanas izmaksas. Praktiski sistēmas testi parāda, ka iegūtā radio teleskopa jutība 1650 MHz frekvencē ir aptuveni 750 Jy. Šajā rakstā tiek izklāstīta uztvērēja galveno komponenšu izstrāde un sniegts svarīgāko parametru praktisks novērtējums.

30.05.2019.

sciendo

LATVIAN JOURNAL OF PHYSICS
AND TECHNICAL SCIENCES
2019, N 3

DOI: 10.2478/lpts-2019-0020

ENVIRONMENTAL PROTECTION

EVALUATION PRINCIPLES OF THE DUST INFLUENCE OF MINING ENTERPRISES ON THE ENVIRONMENT

Semen G. Gendler[1], Marat L. Rudakov[1]*, Vladimir S. Kuznetsov[2]
[1]Department of Industrial Safety
Saint-Petersburg Mining University
199106, 2 21st Line, St. Petersburg, RUSSIA
[2]Department of Geoecology
Saint-Petersburg Mining University
199106, 2 21st Line, St. Petersburg, RUSSIA
*e-mail: Rudakov_ML@pers.spmi.ru

It has been noted that the areas disturbed by open-pit mining together with the production processes in the extraction of mineral resources (drilling, blasting, transportation, etc.) have a negative influence on the environment in general and the atmosphere in particular. It has been indicated that, in percentage terms, dusting of refuse dumps and tailing dumps plays a prevailing role in the total amount of dust generated. It has been stated that the processes of formation and subsequent transfer of dust in the atmosphere depend on the combination of meteorological and mining factors that have a probabilistic nature in time and space. It has been shown that the maximum value of environmental risk characterises the level of dust influence, at which reduction environmental protection measures should be directed. The present paper proposes a procedure for evaluation of the dusty influence of mining enterprises on the environment. Under the conditions of Olenegorsk GOK, a GIS has been compiled – a project of the study area and, based on geo-information modelling, the results of calculating dust concentrations in the air have been imposed on a digital map of the area.

Keywords: *dust influence, GIS modelling, open cast mining, population intoxication risk, refuse dumps, tailing dumps*

1. INTRODUCTION

The development of deposits by the open method is accompanied by negative influence on the environment, which, first of all, leads to deep and areal disturbances of the natural landscape, changes in hydrometeorological conditions in the area of the open-pit mining, movement of poor breeds or even rocks containing harmful

components to the day surface. With an average coal mine of 1,000–2,500 hectares and an iron ore open pit of average thickness of 2,000–3,000 hectares, the total area of disturbed land is 3–12 times greater than the area of the open-pit mining itself, as it includes land occupied by external dumps, industrial sites, transport and energy communications tailing dumps. According to [1], already in 2000, the area disturbed by mining operations in the territory of the Russian Federation amounted to 1,282.6 thousand hectares.

Territories disturbed by open-pit mining together with the production processes in the extraction of minerals (drilling, blasting, transportation, etc.) [2] have a negative impact on the environment in general and on the atmosphere in particular. For example, iron ore enterprises of the European part of Russia annually emit about 94 thousand tons of pollutants, including 60.8 thousand tons of inorganic dust [2]–[5]. A similar situation occurs in a number of foreign open-pit mines [6]–[11].

Sources of inorganic dust formation, in addition to drilling, massive explosions, pit roads, are places for storage overburden (internal and external dumps) and tailing dumps. Moreover, the percentagewise dusting of dumps and tailing dumps play the most important role in the total amount of dust produced.

The characteristic of the formation process and subsequent transfer of dust in the atmosphere is that the factor determining the spatial distribution of dust concentration, under other equal conditions, is the speed and direction of the wind.

On the other hand, the concentration of dust determines the magnitude of the environmental risk and the risk of chronic intoxication of the population living in the area of dust cloud distribution and dust settling on the surface of the earth [12]–[17]. In the present article, an attempt is made to establish a relationship between the magnitude of the dust influence, environmental risk and the risk of population intoxication.

2. METHODOLOGY

Inorganic dust generated as a result of the interaction of atmospheric air flows with the surface of dumps and tailing dumps extends over considerable distances. The distribution of its concentration in atmospheric air is complex determined by the meteorological conditions (temperature, humidity, wind speed and direction) and mining engineering features (physical and mechanical properties of rocks, the geometric sizes of dumps and tailing dumps, their location relative to the contour of the open-pit mining and the wind rose). Dropping from the atmospheric air to the surface of the earth, chemical elements contained in the dust have a depressing effect on water, soil, vegetation, forests, etc. [15].

The processes of formation and subsequent transfer of dust in the atmosphere depend on the combination of meteorological and mining-technical factors that are probabilistic in time and space. Meanwhile, the existing methods for evaluating these processes are based on the use of a deterministic approach, which uses a specific set of initial data for calculating the magnitude of the influencing factor, the choice of which is not always justified [17]. This, ultimately, can lead to a distorted valuation

of the negative impact of the dust generated during the open-pit mining of mineral resources on the environment and, consequently, to errors in the choice of strategy for the implementation of environmental protection measures.

In this regard, it is proposed to calculate the final indicators of dust influence (dust load), taking into account random laws, the changes in the determining factors: speed and direction of wind, air temperature, frequency of mass explosions, the amount of simultaneously explosive and its composition, flow diagrams and drilling modes, types of applied vehicles, their parameters and technological schemes of loading and delivery of minerals and host rocks, places of waste dumps and tailing dumps etc. [18]. The solution of this problem can be fulfilled in the following sequence:

1. At the first stage, the type of statistically distributed laws of factor change determining the level of dust load is established and, on their basis, the probabilities pi of value equality of each of the determining factors to a specific value of vi are calculated. For example, the probability that the air velocity will be equal to *V1* is *p1*, the probability that the air temperature equals the temperature $T_1 - p_2$, the probability that the angle of wind direction is equal to $Y - p_3$, the probability of the frequency of mass explosions to the frequency $K_1 - p_4$, etc. [16].
2. If we assume that the situation in which the above given parameters become equal to specific values forms independent events in aggregate, then the probability of their combination is $\Sigma P_j = \prod_1^n p_i$ (n is the total number of factors taken into account when calculating the final value of the dust load value, i.e., the concentration of dust, gas, etc., *j* – the sequence number of the combination of source data).
3. At the given combination of initial data characterising the factors under consideration, based on the UPRZA Ecolog program [11], numerical values are established characterising the dust load, for example, the contrast ratio Cj, equal to the ratio of the calculated dust concentration to the maximum allowable concentration [18]. The probability of the dust load achievement of the calculated value of Cj will be ΣPj *(j = 1, 2, 3 ……)*.

   If it turns out that the value of *Cj* (or a value close to it) is achieved with different m combinations of the original data, the total probability of reaching the dust load value of the calculated value of *Cj* will be $m\Sigma Pj$.
4. After the completion of the numerical experiment in the coordinates *Cj*, ΣPj, the probability distribution function of the random variable *Cj* is constructed.

3. RESULTS AND DISCUSSION

The level of dust influence (the numerical value of *Cj*) will determine the ecological damage (the effects of technogenic impact expressed in value form), which is applied to the environment, including human health as a result of mineral

extraction. In this case, the larger the absolute value of *Cj*, the greater the magnitude of environmental damage. On the other hand, each value *Cj* is realised with a certain probability, which will have a minimum value in cases of minimum and maximum values *Cj*. In this regard, the integral indicator that determines the level of dust load should be considered the environmental risk calculated as the product of environmental damage and the probability of its occurrence [13]. The maximum value of environmental risk characterises the level of dust exposure, and environmental protection measures should be directed to reduce it [19]. The establishment of a specific set of these measures will be related to the number of influencing factors and the degree of their influence on the final value of *Cj*. In this case, the compensation of factors determined by the peculiarities of the extraction of a mineral (controlled factors) should be carried out by direct influence on the technological processes determining them.

The maximum value of environmental risk in the case when the dust cloud reaches places of compact residence of people will correspond to the maximum risk of chronic intoxication of the population, the value of which, depending on the ratio of the actual concentration of harmful substances in the air to the maximum allowable concentration and hazard class of the substance, looks the following way [18]:

$$R = 1 - ex\,p\left(-0.174\frac{C^b}{K_3 C_{mpc}}\right), \tag{1}$$

where C – the concentration of the pollutant, mg/m^3; C_{mpc} – the maximum permissible concentration of the substance in question, mg/m^3; b and K_3 – coefficients taking into account the toxic properties of the substance.

For the development of environmental measures, environmental action to reduce the risk of intoxication of the population, information is needed on its distribution over the territory adjacent to dusty surfaces: overburden rocks and tailing dumps [20].

Valuation of the dusty impact of open-pit mining on the environment was carried out on the basis of Olenegorsk GOK. The procedure for zoning a territory by the magnitude of technological risk can be carried out as follows. First, the calculation of the inorganic dust concentration distribution over the area of the study territory was performed. For this purpose, the software complex "UPRZA Ecologist" [13] was used. Then a GIS project was formed, with the help of which the results of calculations on the distribution of the inorganic dust concentration were processed and areas were allocated, which were characterised by the magnitude of technogenic risk exceeding the safe value [21]. The implementation of the GIS project was carried out on the basis of the Surfer software package [22]. For the conditions of Olenegorsk GOK, the determination of the level of dust influence was carried out for the overburden dump, having an area of 53 hectares, height of 150 m, and moisture content of stored rocks of 8.1–9 %. First, the amount of inorganic dust emitted from the surface of the blade was calculated, and then the area of inorganic dust distribution was calculated. For further data processing, a GIS was formed – a

project to the site, which was a rectangle with length of 13.8 and width of 9 km. The total area of the study area was 124.2 km^2.

As a result of the numerical implementation of this GIS – areal project, the spatial distribution of technological risk was also established (Figs. 1 and 2).

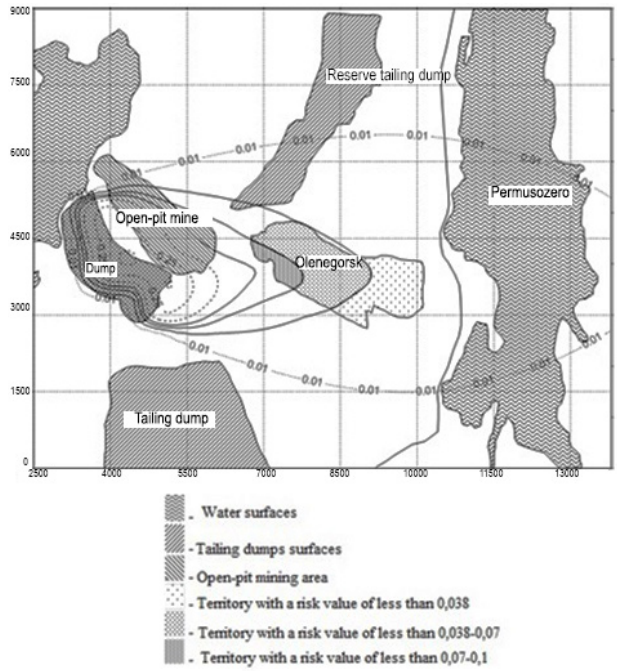

Fig. 1. Area distribution of the technogenic risk (isolines correspond to specific risk values).

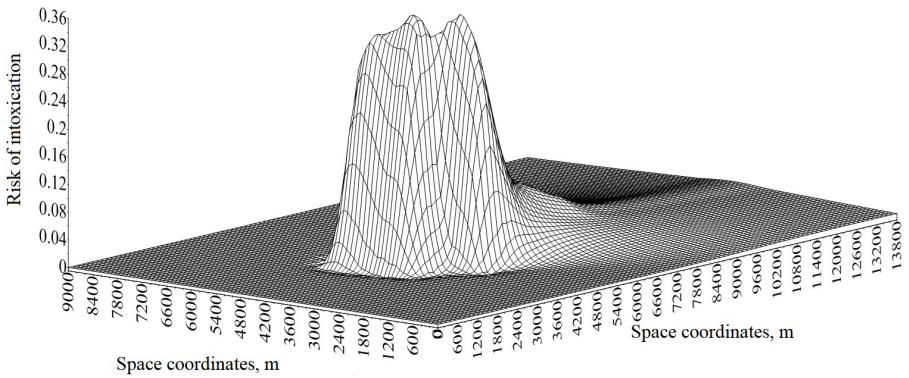

Fig. 2. Space distribution of the technogenic risk.

Based on the map (Fig. 1), the zoning of the territory occupied by Olenegorsk was made in accordance with the risk values (Table 1).

Table 1

Differentiation of the Territory of Olenegorsk Depending on the Magnitude of the Risk

R	Area size, m^2	%
0.1 – 0.07	353394	10
0.07 – 0.038	1850023	51
Less than 0.038	1389637	39

Analysis of the data presented in Table 1 suggests that the dust influence of overburden dumps leads to the following negative consequences:

- 10% of the territory of Olenegorsk is in the area of technogenic risk, which determines the possibility of toxic effects with a probability of 0.07 – 0.1.
- 51% of the area of Olenegorsk belongs to the field of technogenic risk, which determines the possibility of toxic effects with a probability of 0.07 – 0.038.
- 39% of the area of Olenegorsk is characterised by technogenic risk values not exceeding 0.038, which corresponds to the concentration of inorganic dust equal to the MPC.

4. CONCLUSIONS

Consequently, in order to evaluate the dust influence of the mining enterprises on the environment, the following stages should be followed:

- establishing the number of influencing factors and random laws of their distribution;
- defining the maximum values of the ecological risk;
- compiling of the GIS project of the study area and the implementation with geo-information modelling the imposition of the calculation results of dust concentrations in the air on a digital map of the area;
- allocating areas characterised by pollution of various levels (C_i / C_{mpc}), and the calculation of the proportion of contaminated areas relative to the total area of the study area;
- establishing areal distribution of risk of population intoxication;
- justifying the strategy of environmental protection measures, taking into account the areal distribution of the risk of intoxication.

REFERENCES

1. Katoria, D., Sehgal, D., & Kumar, S. (2013). Environment impact assessment of coal mining. *International Journal of Environmental Engineering and Management*, *4*(3), 245–250.
2. Hughes, D.J., Shimmield, T.M., Black, K.D., & Howe, J.A. (2015). Ecological impacts of large-scale disposal of mining waste in the deep sea. *Scientific Reports*, *5*, 9985.
3. Saik, P.B., Dychkovskyi, R.O., Lozynskyi, V.H., Malanchuk, Z.R., & Malanchuk, Ye.Z. (2016). Revisiting the underground gasification of coal reserves from contiguous seams. *Naukovyi Visnyk Natsionalnoho Hirnychoho Universytetu*, *6*, 60–66.

4. Volkodaeva, M.V., & Kiselev, A.V. (2017). On development of system for environmental monitoring of atmospheric air quality. *Journal of Mining Institute*, *227*, 589–596.
5. Maheshi, D., Van Passel, S., & Van Acker, K. (2015). Environmental and economic assessment of 'open waste dump' mining in Sri Lanka. *Resources, Conservation and Recycling, 102*, 67–79.
6. Kowalska, I.J. (2014). Risk management in the hard coal mining industry: Social and environmental aspects of collieries' liquidation. *Resources Policy*, *41*(1), 124–134.
7. Grujić, M. (2010). Possibilities for environmental protection application of belt conveyors with horizontal curves in the mines of coal. *The International Journal of Transport & Logistics*, *10*(7), 243–247
8. Chugh, Y.P., & Behum, P.T. (2014). Coal waste management practices in the USA: an overview. *International Journal of Coal Science and Technology*, *1*(2), 163–176.
9. Ondar, S.O., Khovalyg, A.O., Ondar, U.V., & Sodnam, N.I. (2018). Monitoring of the state of the left-bank confluents of the Upper Yenisei basin in the zone of impact of the coal industry enterprise. *International Journal of Engineering and Technology (UAE)*, *7*(3), 206–214.
10. Ghose, M.K, & Majee, S.R. (2007). Characteristics of hazardous airborne dust around an Indian surface coal mining area. *Environmental Monitoring and Assessment, 130*, 17–25.
11. Sharma, P.K, & Singh, G. (1992). Distribution of suspended particulate matter with trace element composition and apportionment with possible sources in Raniganj coalfield India. *Environmental Monitoring and Assessment*, *22*, 237–244.
12. Firm "Integral". (2017). *Methods for calculating the dispersion of emissions of harmful (polluting) substances in atmospheric air*. Available at https://integral.ru/shop/cargo/386.html
13. Alymov, V.T., Krapchatov, V.P., & Tarasova, N.P. (2014). *Analysis of technological risk.* Moscow: Kruglyy god.
14. Murzin, M.A. (2016). Mining enterprises as a source of environmental risks. *Mining Information and Analytical Bulletin, 2*, 374–383.
15. Dychkovskyi, R.O. (2015). Determination of the rock subsidence spacing in the well underground coal gasification. *Naukovyi Visnyk Natsionalnoho Hirnychoho Universytetu*, *6*, 30–36.
16. Kalybekov, T. Zhakypbek, Y. Tursbekov, S.V., & Tursbekova, G.Zh. (2014). Problems of geo-ecological risk assessment in the open mining of mineral deposits. *Mountain Journal*, *4,* 64–70.
17. Pivnyak, G., Dychkovskyi, R., Smirnov, A., & Cherednichenko, Yu. (2013). Some aspects on the software simulation implementation in thin coal seams mining. In *Energy Efficiency Improvement of Geotechnical Systems – Proceedings of the International Forum on Energy Efficiency* (pp. 1–10). London: CRC press.
18. Pashkevich, M.A., & Strizhenok, A.V. (2012). Reducing the negative impact of man-made arrays on the quality of atmospheric air. In *Proceedings of the 8th International Conference on Mining, Construction and Energy "Socio-economic and environmental problems of the mining industry, construction and energy*" *Vol. 2.* (pp. 299–306). Tula: TSU.
19. Aleksandrov, V.M., Golozubenko, E.S., Ponomarev, S.A., & Saltykov, V.V. (2018). Detachment of alluvial paleofacial complexes in the upper Jurassic deposits of the South-West of the West Siberian oil and gas basin. *Periodico Tche Quimica, 15*(S1), 265–275.
20. Mironova, S.I., Ivanov, V.V., Gavrilyeva, L.D., & Nikiforov, A.A. (2018). Persistence of Yakutia vegetation under the technogenic impact. *Periodico Tche Quimica*, *15*(S1), 18–26.

21. Krasovskaya, O., Skaterschikov, S., Tyasto, S., & Khmefea, D. (2003). GIS in the system of territorial planning and management of the territory. *ArcReview*, *3*(38), 106–112.
22. Ivanova, I.A., & Chekantsev, V.A. (2008). *Solving geological problems using the Surfer software package: A workshop for students in the field of Applied Geology.* Tomsk: Publishing House of Tomsk Polytechnic University.

KALNRŪPNIECĪBAS UZŅĒMUMU PUTEKĻU IETEKMES UZ VIDI NOVĒRTĒŠANAS PRINCIPI

S. G. Gendlers, M. L. Rudakovs, V. S. Kuzņecovs

K o p s a v i l k u m s

Teritorijas, kur notiek atklāta derīgo izrakteņu ieguve, kā arī ražošanas procesi, kas saistīti ar derīgo izrakteņu ieguvi (urbšana, spridzināšana, transportēšana u.c.), negatīvi ietekmē apkārtējo vidi un it īpaši atmosfēru. Atkritumu izgāztuvju putekļu noņemšanai ir dominējošā loma kopējā saražoto atkritumu procentuālā apjomā. Putekļu veidošanās procesi atmosfērā ir atkarīgi no meteoroloģiskajiem un kalnrūpniecības faktoriem, kuriem ir varbūtības raksturs laikā un telpā. Pierādīts, ka vides riska maksimālā vērtība raksturo putekļu iedarbības līmeni, kas ir jāņem vērā vides aizsardzības pasākumu īstenošanai. Rakstā piedāvāta procedūra, kā novērtēt kalnrūpniecības uzņēmumu ietekmi uz vidi. Oļeņegorskas ieguves un pārstrādes rūpnīcas apstākļos sastādīts ĢIS – pētījuma projekts un, pamatojoties uz ģeoinformācijas modelēšanu, putekļu koncentrācijas gaisā aprēķināšanas rezultāti ir uzlikti uz teritorijas digitālās kartes.

18.03.2019.